PHYSIK DEPARTMENT

TECHNISCHE UNIVERSITÄT MÜNCHEN
MAX PLANCK INSTITUTE FOR EXTRATERRESTRIAL PHYSICS

Bachelor's Thesis in Physics

Measuring the Light Curve of the Crab Nebula

Messung der Lichtkurve des Krebsnebels

Author:	Joachim Thomas Ziegler
Supervisor:	Dr. Jochen Greiner
Advisor:	Dr. Thomas Siegert
Submission Date:	06.09.2022

Contents

1. Introduction

The Crab Nebula, henceforth also just Crab, is one of the best known supernova remnants and pulsar wind nebulae. First discovered in 1731 by John Devis (Hester 2008), the Crab is one of the brightest and steadiest X-ray sources on the night sky and therefore used as calibration source for different measurement instruments in the X- and γ-ray domain. To check the Crab's reliability as so called *standard candle*, several instruments monitor its light flux and spectral behavior over time. Instruments for this purpose are the *Fermi* Gamma-ray Burst Monitor (GBM), the *Swift* Burst Alert Telescope (*Swift*/BAT), the *Rossi X-ray Timing Explorer* Proportional Counter Array (*RXTE*/PCA), or the *INTErnational Gamma-Ray Astrophysics Laboratory* (*INTEGRAL*) (Wilson-Hodge et al. 2011). INTEGRAL is measuring the Crab for a small time period twice a year since its launch in October 2002. The Spectrometer on INTEGRAL (SPI) is one of its main instruments and consists of 19 germanium detectors to detect single photons in the hard X-ray and soft γ-ray energy domain (20 keV to 8 MeV). These detectors encounter interaction events with photons and measure the energy deposited in the detector and the interaction time, which allows for a spectral analysis and the construction of light curves (Jourdain and Roques 2020).

In this Bachelor's thesis, I examine whether the Crab can be treated as a standard candle. To answer this question, I analyze the data gathered by SPI since the start in 2002 until 2018 using the INTEGRAL Offline Scientific Analysis (OSA) software (Courvoisier et al. 2003). In that process, I construct a light curve of the Crab flux and examine a spectral analysis using different spectral models to investigate the Crabs flux variability. As recent results from Jourdain and Roques (2020) showed a lot of variability in the Crab emission, a further analysis of the Crab data is valuable to confirm its status as standard candle in the X- and γ-ray domain.

Most of the information about the universe is transmitted via cosmic radiation. However, this results in a substantial problem in the X- and γ-ray data analysis, in particular the MeV energy range, because the data samples are obscured by a considerable amount of instrumental background photons. Hence, it is necessary to decide which photons belong to the source measured by the satellite, and which photons have to be considered to be part of the background noise. This is done by building and applying a *background model* (Siegert et al. 2019). To further extract the spectral information, statistical methods are applied. In my thesis the *Maximum Likelihood Method* and a method based on *Bayesian Statistics* are used to fit the model to the data. Through several scripts within the OSA software, the statistical methods are implemented.

Recent papers by Wilson-Hodge et al. (2011) and Jourdain and Roques (2020) analyzed the data received from the Crab and gave reason that the widely-held assumption that the Crab can be used as a standard candle should be treated with caution. Wilson-Hodge et al. (2011) examined data from Fermi, Swift, RXTE and INTEGRAL and found a decline of the Crab flux of $\sim 7\%$ in the 15–50 keV energy band and a similar decline in the 50–100 keV energy band over a two year period starting at MJD 54690—the 12th of August 2008—independent of the instrument. The fact that all instruments use different observing techniques, reassures that the variations at a level of approximately 3.5 %/yr are intrinsic to the Crab. Furthermore, Jourdain and Roques (2020) observed the Crab Nebula with data from SPI over a long-term scale (2002–2020) and found that the Crab flux variability is contained within less than ±5% around a approximately 20 yr mean value for broad bands covering the 20–400 keV energy domains. The weak flux limits a meaningful interpretation for higher energy bands. Additionally, Jourdain and Roques (2020) inspected the spectral shape and found that a smoothly broken power-law function, first introduced by Band et al. (1993) and henceforth known as *Band function*, provides a good description of the Crab emission in the energy range of 20–2200 keV.

As the status of the Crab as standard candle is so important for the high-energy astrophysics, I compare my results for compatibility with the preceding results of Wilson-Hodge et al. (2011) and Jourdain and Roques (2009) and Jourdain and Roques (2020). My results are important due to several reasons. First, with the OSA software I use a different software than Jourdain and Roques, including a different background model. Second, due to the different analytical methods applied, the high-energy domain can be better analyzed because the spectral model I am using is better constrained.

The structure of this thesis is as follows: First, I provide some necessary background knowledge about the origin, discovery and what is unique about the Crab in Section 2. Afterwards, I explain the functionality of INTEGRAL and especially SPI in Section 3. Thereafter, I outline the data analysis methods used in Section 4. Next, I present my results of the light curves constructed and the spectral analysis in Section 5. Lastly, I compare my findings with the previous papers by Wilson-Hodge et al. (2011), Jourdain and Roques (2009), and Jourdain and Roques (2020) in Section 6. Section 7 concludes the thesis.

2. The Crab Nebula

The Crab Nebula is a 3.4 pc wide remnant of the historical supernova of 1054 AD (Hester 2008). With its distance of roughly 2000 pc (Hester 2008) from Earth, visible in the constellation of Taurus, it is the brightest, and presumably most constant X- and γ-ray source. Figure 1 shows an image of the Crab Nebula taken by the Hubble Space Telescope in 2005. In the following section, first the stellar evolution from protostar to neutron star and stellar nebula is explained, next a short insight in the history of the discovery of the Crab is sketched and afterwards the uniqueness of the Crab is discussed.

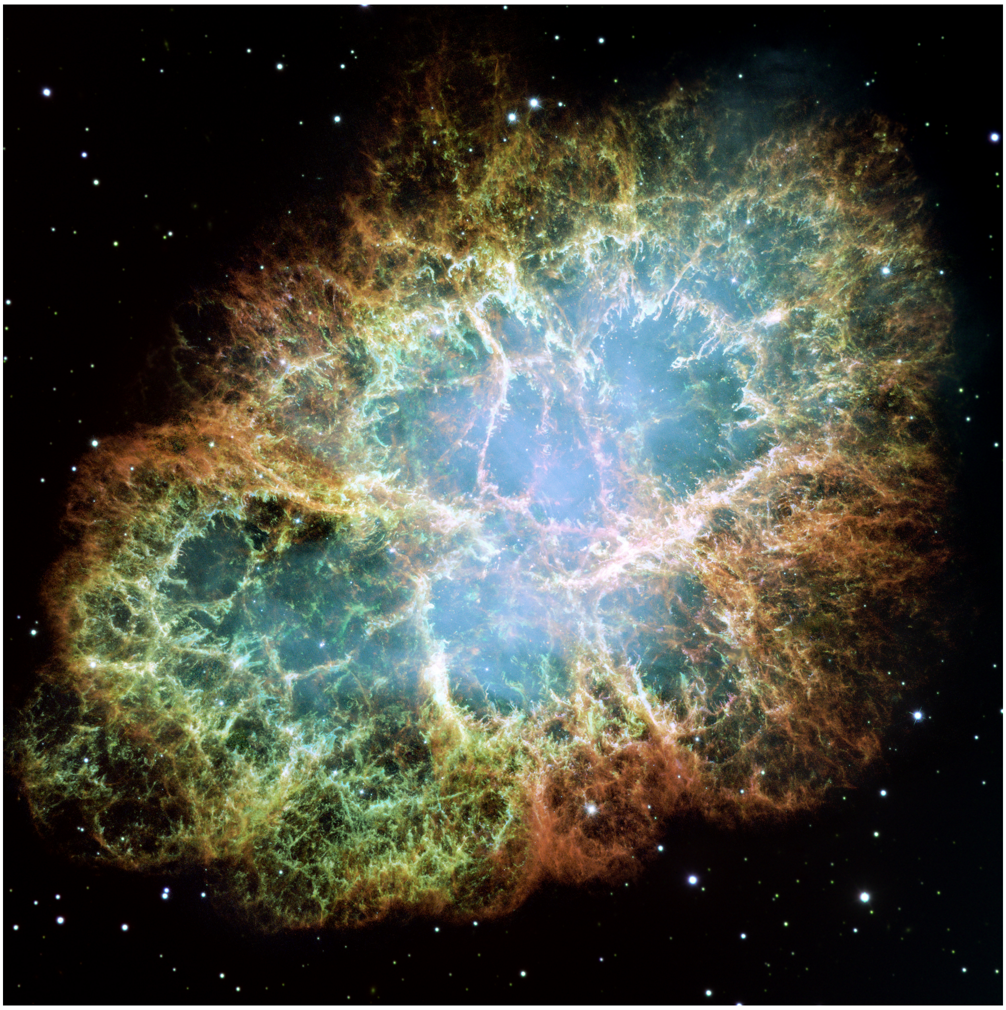

Figure 1: This image taken by the Hubble Space Telescope gives the most detailed view of the entire Crab Nebula ever taken. It was assembled from 24 individual exposures taken with the Hubble Space Telescope's WFPC2 camera (NASA, ESA, et al. 2005). The different colors show the chemical composition of the thermal filaments composed of ejecta from the explosion. Blue indicates neutral oxygen [O I, $\lambda = 631\,\mathrm{nm}$], green is singly-ionized sulfur [S II, $\lambda = 673\,\mathrm{nm}$], and red represents doubly-ionized oxygen [O III, $\lambda = 502\,\mathrm{nm}$] (Hester 2008; NASA, ESA, et al. 2005).

2.1. Stellar Evolution

Stars evolve on the timescale of millions to billions of years depending on the mass. The larger its mass, the shorter its life cycle. Figure 2 illustrates possible evolutionary pathways for the life cycle of stars. A new star forms with the gravitational force pulling matter from the remnant of stars, which already completed their life cycle, together. The more matter in this *nebula*—a giant cloud of gas and dust—is available, the more mass a star can gather. Gravity pulls the hydrogen gas together over time and the gas begins to spin due to angular momentum conservation, accelerates, and heats up until it becomes a *protostar* (Hanslmeier 2014, p. 378 sqq.).

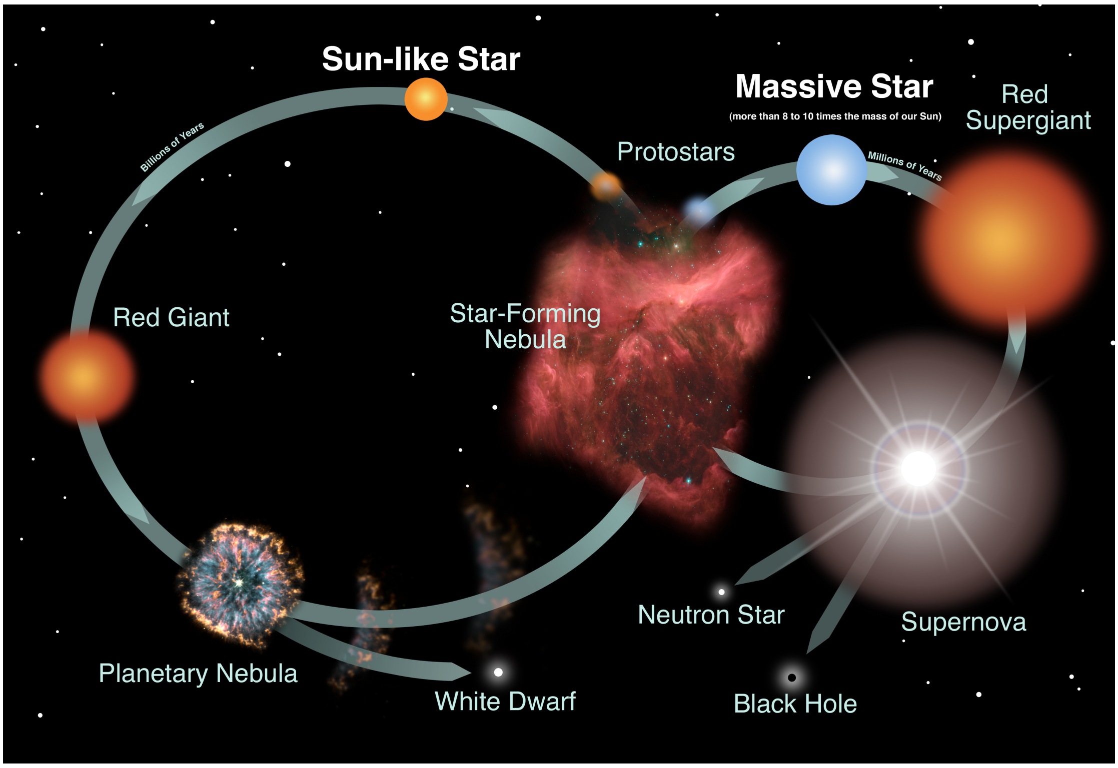

Figure 2: Artist impression of some possible evolutionary pathways for the life cycle of stars for different initial masses (NASA and Night Sky Network 2009).

At temperatures of 15×10^6 K nuclear fusion sets in in the protostar's core, and it begins to glow brightly, and contracts slightly, and becomes stable forming an equilibrium between the gravitational force and the radiation pressure. The star now enters the longest part of its life as a *main sequence star* and remains in this stage for about

80% of its life time burning its fuel. In this process hydrogen in the core fuses to helium in the so-called *hydrogen-burning*. Many different nuclear fusion processes are possible, like proton-proton chains (pp), deuterium fusion, and the carbon-nitrogen-oxygen (CNO) cycle. However, due to simplicity reasons, I will stick to the most important one, showing only the *proton-proton-I-chain* (pp1) (Hanslmeier 2014, p.366 sqq.):

$$
\begin{aligned}
{}^{1}\mathrm{H} + {}^{1}\mathrm{H} &\rightarrow {}^{2}\mathrm{H} + e^{+} + \nu_e && (1)\\
{}^{2}\mathrm{H} + {}^{1}\mathrm{H} &\rightarrow {}^{3}\mathrm{He} + \gamma && (2)\\
{}^{3}\mathrm{He} + {}^{3}\mathrm{He} &\rightarrow {}^{4}\mathrm{He} + 2\,{}^{1}\mathrm{H}. && (3)
\end{aligned}
$$

The pp1-chain is also shown in Figure 3. After nearly all hydrogen in the core is converted to helium, the star expands slightly as the core temperature rises and its luminosity increases. While in the next outer shell hydrogen continues burning to helium, helium starts burning in the core. In this process the core contracts, leading to a greater energy production and an increase of temperature of the hydrogen burning shell and the star starts to expand considerably. Following this, the surface temperature

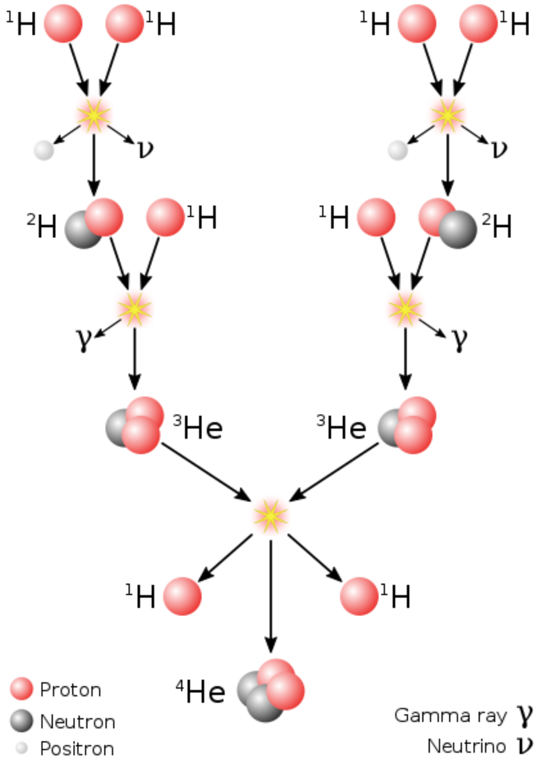

Figure 3: Scheme of the proton–proton branch I (pp1) reaction (Sarang 2016).

decreases making the star shine red and thereby becoming a *red giant star* (Hanslmeier 2014, p. 378 sqq.). The helium burning mainly happens through the *triple-alpha process* leaving behind a carbon-rich core (Hanslmeier 2014, p.366 sqq.):

$$^{4}\mathrm{He} + {}^{4}\mathrm{He} \rightarrow {}^{8}\mathrm{Be} \tag{4}$$

$$^{8}\mathrm{Be} + {}^{4}\mathrm{He} \rightarrow {}^{12}\mathrm{C} + \gamma. \tag{5}$$

All stars evolve the same way up to the red giant phase. Afterwards the mass of a star determines which life cycle path the star will take, cf. Figure 2. Stars with similar or less mass than the sun end as *white dwarfs* with a different elemental composition depending on the initial mass. They are not hot enough to reach silicon-burning (equation (9), so the core collapses as soon as all fuel is used up and the outer layers of the star are expelled forming a expanding envelope called *planetary nebula* (Hanslmeier 2014, p. 378 sqq.).

Especially more massive stars are important to understand the origin of the Crab Nebula. Hence, we will look at their life cycle path more in detail. Massive stars ($> 8M_\odot$) reach high enough temperatures ($\sim 3 \times 10^9$ K) in the core to burn elements up to iron (^{56}Fe). In this temperature regions many different processes are possible (Hanslmeier 2014, p. 378 sqq.). Equation (6) to (9) show common processes of carbon-, neon-, oxygen- and silicon-burning (Hanslmeier 2014, p.366 sqq.). ^{56}Fe has the highest binding energy per nucleon of all elements. Consequently, further nuclear fusion of iron would not release energy, so the burning ceases when iron is reached.

$$\text{Carbon-burning:} \quad {}^{12}\mathrm{C} + {}^{12}\mathrm{C} \rightarrow ... \rightarrow {}^{20}\mathrm{Ne} + {}^{4}\mathrm{He} + \gamma \tag{6}$$

$$\text{Neon-burning:} \quad {}^{20}\mathrm{Ne} + \gamma \rightarrow {}^{16}\mathrm{O} + {}^{4}\mathrm{He} \tag{7}$$

$$\text{Oxygen-burning:} \quad {}^{16}\mathrm{O} + {}^{16}\mathrm{O} \rightarrow ... \rightarrow {}^{28}\mathrm{Si} + {}^{4}\mathrm{He} + \gamma \tag{8}$$

$$\text{Silicon-burning:} \quad {}^{28}\mathrm{Si} + {}^{28}\mathrm{Si} \rightarrow {}^{56}\mathrm{Fe} \tag{9}$$

In the end of the evolution, stars consist of an 'onion-like' structure with an iron core in the center followed by a silicon shell and so on. Figure 4 shows a schematic illustration.

Once all the fuel of a massive star is consumed, the equilibrium between gravitational force radiation pressure breaks down. If the mass of the iron core surpasses the Chandrasekhar limit of $1.4M_\odot$ (Hanslmeier 2014, p. 389 sqq.), gravity wins the battle and the star collapses without opposition. In the course of this, the density in the center of the star gets higher and higher until all the pressure from the collapse is released at once in single extremely powerful burst, a so-called *Supernova* (Hester et al. 1996). During the explosion the outer layers are thrown off and the core compresses even more. While the ejected outer layers of expanding dust and gas become a *supernova*

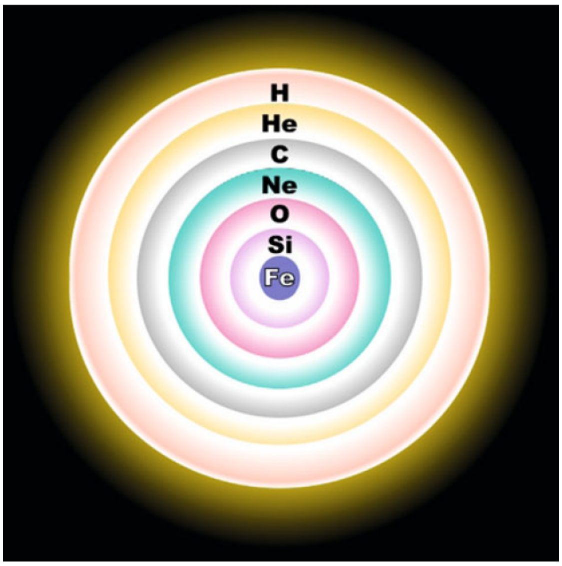

Figure 4: The 'onion-like' structure of a massive star at the end of its development (Hanslmeier 2014, p.386). The core consists of iron, followed by silicon, oxygen, neon, carbon, helium and hydrogen in the surrounding shells up to the stars surface.

remnant, the core is left behind as a *neutron star*. If the mass of the iron core even surpasses the Tolman–Oppenheimer–Volkoff limit (estimates lie somewhere between 3 and 4 $M_\odot$ according to Hanslmeier (2014)) the object collapses to a black hole.

A neutron star is the relic of the star's core and emerged from the compression of protons and electrons to a single exorbitantly dense object made of neutron matter. Consequently, neutron stars are really small just in the size of cities ($\sim$10 km wide), but posses greater mass than the Sun. That also leads to excessive gravitational fields about 300 000 times stronger than the Earth's field (Hester et al. 1996). Furthermore, due to the conservation of angular momentum, the rotation of the star dramatically increases during the collapse, when the size of the star shrinks to just a few kilometers in width. Rapidly rotating neutron stars emit radio waves, and often other forms of radiation on the electromagnetic spectrum, giving them the name *pulsar* (for pulsating radio source) (Hester et al. 1996; Roberts et al. 2005, p. 249). Due to the spin of the star, the radio waves are only measured when the pulsar's beam hits Earth making it appear to turn on and off. The main difference between a neutron star and a pulsar is that latter has a misaligned magnetic field compared to the rotation axis being tilted at an angle of about 30° (Hester et al. 1996). This results in emission of synchrotron radiation from the magnetic poles. The powerful magnetic field of the pulsar traps and accelerates charged particles close to the speed of light. These charged particles interact with the surrounding gas of the supernova remnant and let the resulting *pulsar wind nebula* light up and expand (Hester et al. 1996; Gaensler and Slane 2006).

2.2. History & Discovery

As explained, a supernova remnant and pulsar wind nebula forms after a high-mass star reached the end of its normal life cycle and exploded in a supernova. Knowing the connection between stars, supernovae and nebulae, we can now take a look at the history and discovery of the Crab Nebula.

On July 4, 1054 AD Chinese astronomers among others discovered a new *guest star* in the constellation of Taurus, which was bright enough to be seen in daylight for over three weeks and at night for 22 months (Hester 2008). With our modern understanding we know now that the *guest star* the astronomers saw back in 1054 was actually a supernova explosion.

The Crab Nebula itself was discovered in 1731 by John Bevis and independently rediscovered in 1758 by Charles Messier. Messier originally mistook the Crab with Halley's Comet and later realised that his found comet is not moving across the sky. Thereafter, Messier started cataloguing comet-like objects in his *Messier catalogue* and the Crab Nebula was named: M(essier) 1 (Hester 2008). Between 1783 and 1809 Sir William Herschel made the next significant observational records of the Crab Nebula, although it is not known if he discovered the Crab independently or knew of its existence due to Messier's catalogue. In his nine surveillances of the Crab, he concluded that the object is most likely a cluster of stars (Mayall 1939). In 1844 William Parsons, third Eral of Rosse, observed the Crab with a 72-inch reflecting telescope and made a drawing of the Crab Nebula which looked like a Crab, leading to the name *Crab Nebula*. The first connection between the Crab Nebula and the supernova of 1054 was proposed by Lundmark in 1921 (Hester 2008) and later in 1928 by Edwin Hubble (Rossi 1969). From the hypothesis that the Crab Nebula had originated from a point-like object and uniformly expanded since then, Hubble could calculate its age, which came close to the appearance of the *guest star*. However, Hubble's results remained obscure as the life cycle of stars, and thus its explosion in a supernova, was not known at his time (Al Dallal, Azzam, et al. 2021). However, not until the work of Duyvendak (1942) and Mayall and Oort (1942) in the publishing of studies of modern observations of the nebula and of the ancient Chinese reports, it got established that the Crab is indisputably corresponding with the *guest star* from 1054 AD (Hester 2008). Today the Crab Nebula is of great interest in nearly every branch of astrophysics and probably the most studied object in the sky next to our own solar system.

2.3. Uniqueness of the Crab

The Crab Nebula consists of the Crab pulsar in the center and the pulsar wind nebula itself enclosing it. The Crab pulsar is one of the youngest and most energetic pulsars known (Hester et al. 1996), making it radiate in the whole electromagnetic spectrum, especially in the X- and γ-ray range. The strong magnetic field of the pulsar accelerates charged particles, which interact with the gas particles of the surrounding nebula, making it emit light in the whole electromagnetic spectrum as well. Due to this process the pulsar looses energy, so that it spins slower over time. This *spin-down rate* is only a tiny percentage per year, but will eventually lead to the Crab's pulses becoming less intense and its X-ray emission will end (Hester et al. 1996). Particularly in the X- and γ-ray range the Crab Nebula is one, if not the brightest and most stable sources (Jourdain and Roques 2009) because of its relatively young age, making the Crab unique. This leads to the Crab supernova remnant to be frequently considered to be a steady standard candle suitable as calibration source (Wilson-Hodge et al. 2011).

3. Description of the Instrument

3.1. INTEGRAL Mission

In October 2002, the INTEGRAL satellite was launched, equipped with several instruments for measurements in the X- and γ-ray region. The satellite orbits Earth in a highly eccentric 72h-orbit with an inclination of 52.2°. Due to the elliptical orbit with a close perigee of 9000 km and a far apogee of 154 000 km long periods of uninterrupted observations with nearly constant background are provided. Measurements are stopped at an altitude of 60 000 km and resumed at an altitude of 40 000 km to avoid disturbances by Earth's radiation belt. This results in more than 80 % of the orbit duration being used for scientific observations (Kretschmar et al. 2005). One full orbit is titled *revolution* (or shortened: rev). Figure 5 shows an illustration of INTEGRAL.

INTEGRAL is equipped with four instruments, which, broadly described, are: The *Imager on board the INTEGRAL satellite* (IBIS), with a field of view of 9° × 9° and an energy range of 15 keV to 10 MeV, is one of the main instruments of INTEGRAL and used for high-angular resolution imagining (Kretschmar et al. 2005). The *Spectrometer on INTEGRAL* (SPI), with a field of view of 16° × 16°, is the second main instrument and used for high-resolution γ-ray line spectroscopy in the hard X-ray and soft γ-ray range between 20 keV and 8 MeV (Kretschmar et al. 2005; Vedrenne et al. 2003; Winkler et al. 2003). The next Section 3.2 contains greater detail about SPI. Furthermore INTEGRAL holds two monitors: The *Joint European X-Ray Monitor* (JEM-X), which operates in an energy range from 4 keV to 35 keV, and an optical monitor camera (OMC) observing

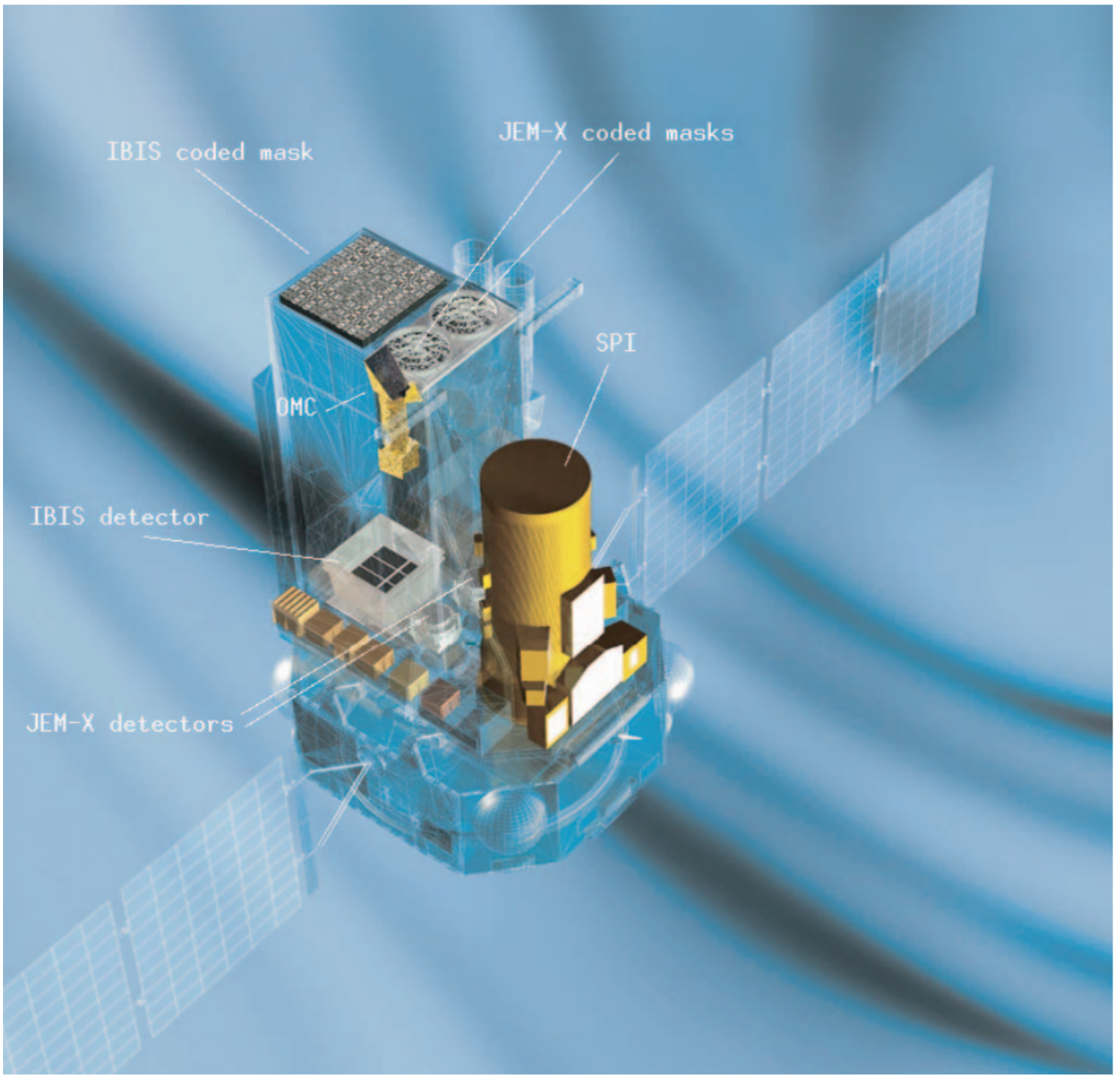

Figure 5: Illustration of the INTEGRAL satellite with the dimensions $5 \times 2.8 \times 3.2\,\mathrm{m}$. The different instruments on board the satellite are marked (Winkler et al. 2003).

wavelengths between 500 nm and 600 nm.

The goal of the INTEGRAL mission is the examination of high energetic phenomena, which can be investigated by γ-ray spectroscopy. With the data provided by SPI and IBIS, the position of X- and γ-ray sources as well as the chemical composition of different objects in the γ-ray line spectrum can be determined over a large energy range. Thus, INTEGRAL offers a perfect instrument to study X-ray sources like Gamma-Ray-Bursts (GRBs) or the Crab Nebula in their spectral behavior and flux intensity.

3.2. Functionality of SPI

The SPI instrument is of special importance for this thesis, as the data provided by SPI was used for the data analysis of the Crab (see Section 5). Figure 6 displays this coded mask telescope.

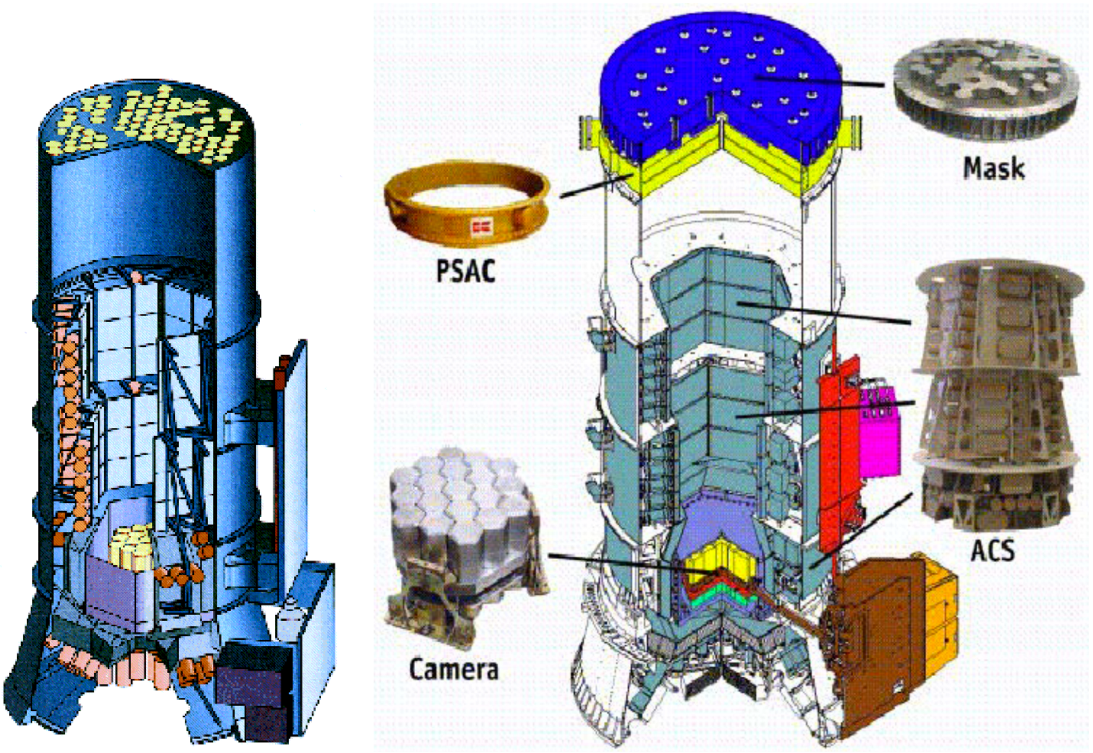

Figure 6: SPI Instrument on Integral. Left: Schematic, Right: Cut-away showing components more clearly (Diehl et al. 2018).

The SPI instrument consists of four main components, the germanium detector array, an anti-coincidence detector system (ACS), a coded tungsten mask to shield the viewing field and a plastic scintillator plate (PSAC). Figure 7 shows the different subsystems.

The germanium detector camera, consisting of 19 individual germanium detectors with a hexagonal shape, represents the most important part of SPI. Due to the hexagonal shape the use of space in the instrument is optimized. Figure 8 demonstrates the scheme of the 19 germanium detectors. Each detector has a side length of 32 mm, a height

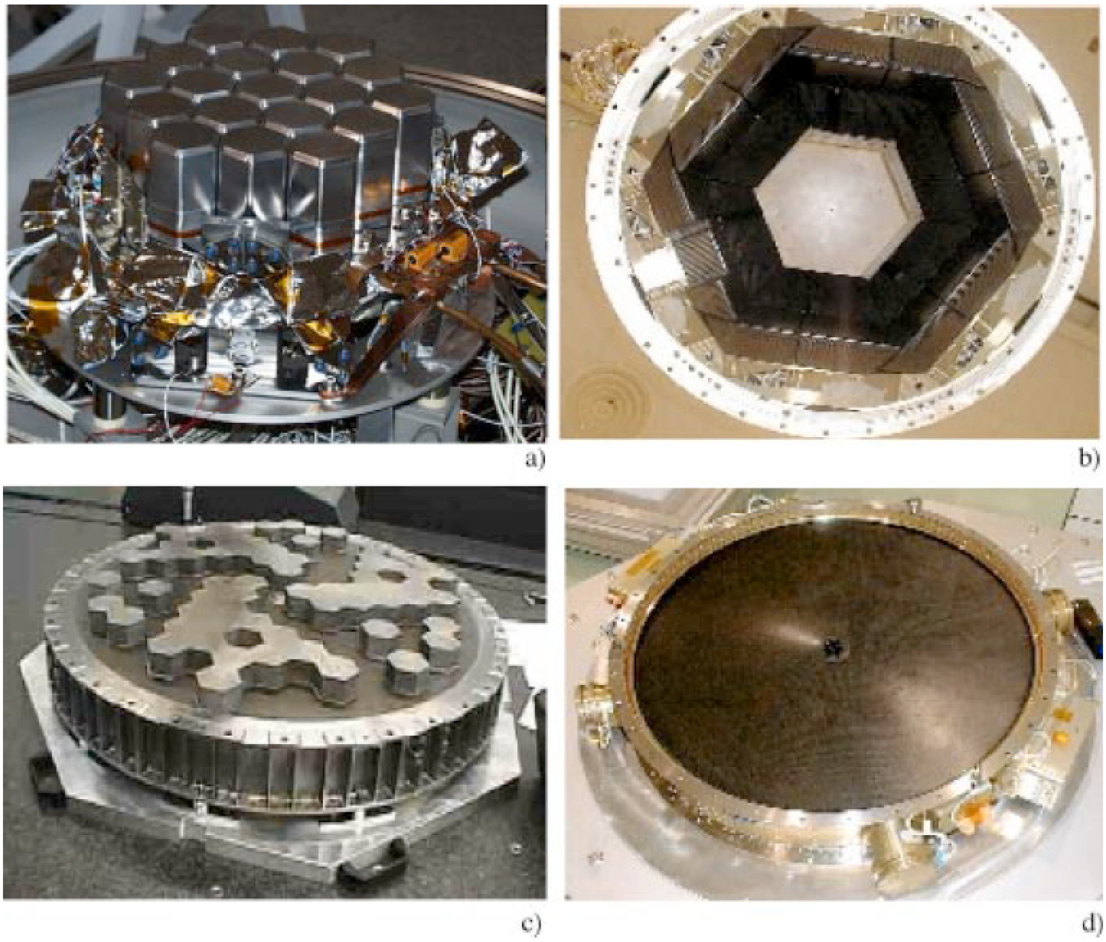

Figure 7: The most important subsystems of SPI: **a)** Array with 19 germanium detectors forming the γ-ray camera; **b)** ACS; **c)** coded mask made out of tungsten to shield the Ge detectors; **d)** plastic scintillator; from Vedrenne et al. (2003).

of 69.42 mm, an external diameter of 60.65 mm, a distance of 56.04 mm from one flat side to the other, and the centers of neighboring cells are 60 mm apart from each other. To increase the sensitivity, the germanium detectors are operated at a temperature of 85 K and actively cooled to reduce the effect of radiation damage on the material (Kretschmar et al. 2005; Vedrenne et al. 2003). Germanium detectors belong to the group of semiconductor diode detectors. Electron-hole-pairs can either be generated by thermal excitation—which is suppressed in SPI due to the active cooling—or when a particle deposits energy in the semiconductor detector. Applying voltage to the detector results in the electron and the hole drifting in opposite directions, constituting two electric currents, which persists until the the charge carriers are collected at the boundaries of the detector. With sufficiently high voltage, the charge carriers are accelerated to high velocities and thereby the collection time is reduced (Knoll 2011).

At a height of 171 cm above the germanium detector array the coded mask, arranged in a circle of 72 cm diameter, is positioned. The tungsten mask with a 120° rotational symmetry and a mass of 140 kg, is made up of 127 hexagonal pixels, 63 of which are opaque and 64 of which are transparent to γ radiation within SPI's energy range (Vedrenne et al. 2003). The mask shields a part of the viewing field of the detectors and therefore leads to a different intensity distribution on each of the individual detectors. Through one or more shadowgrams with different viewing angles and thereby different intensity distributions the location of γ-ray point sources is determined by the direction they arrive within the field of view (FoV) of SPI. Exemplary shadowgrams with a variation of the viewing angel in steps of 2.1° are shown in Figure 9 (Diehl et al. 2018). 2.1° is the normal reorientation of SPI every 30 min; for the time in between it stares.

The Anti-Coincidence detector system (ACS) is surrounding the hole composition, to filter events originating from prompt cosmic-ray interactions and consists of 91 BGO crystals. The Plastic Scintillator Anticoincidence subassembly (PSAC) is a thin scintillator plate directly below the tungsten mask and allows the rejection of background induced by these prompt cosmic-rays in the mask. Due to a 70 cm gap between mask and ACS, the particles to not reach the BGO crystals (Vedrenne et al. 2003).

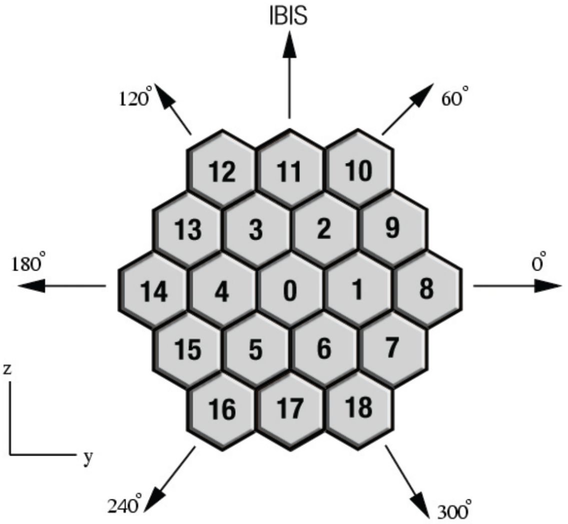

Figure 8: Hexagonal configuration of the 19 germanium detectors on the SPI camera (Diehl et al. 2018).

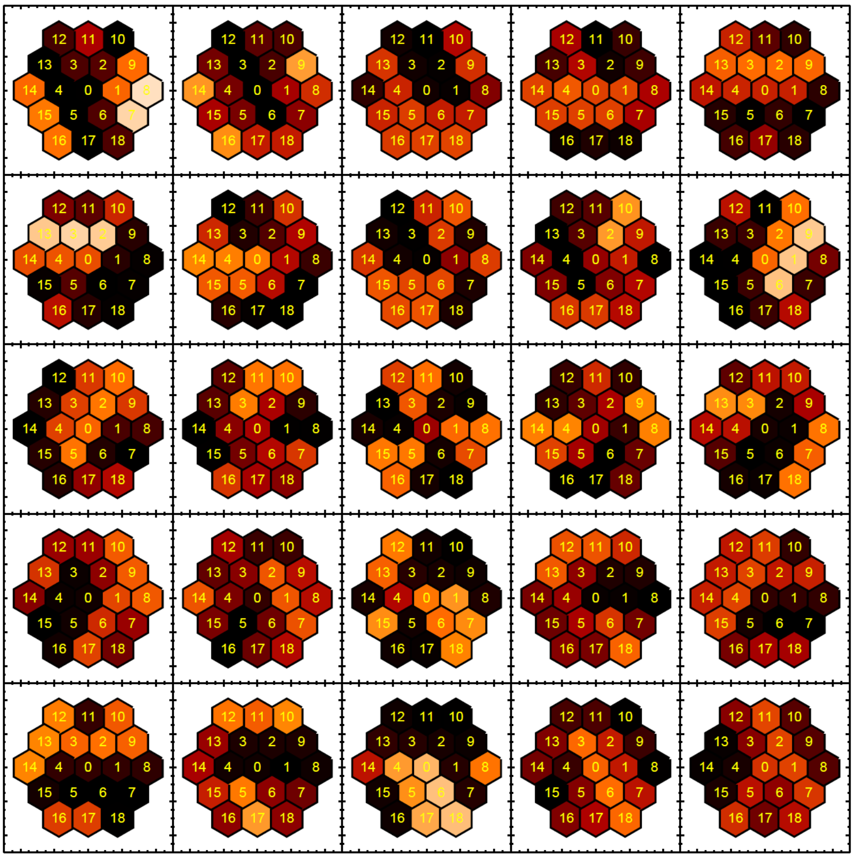

Figure 9: Exemplary shadowgrams of the 19 germanium detectors for a point source on axis during 25 pointings, with a reorientation of the telescope of 2.1° per pointing. The measured intensity by each detector is colour-coded from white (full exposure) through yellow and red to black (no radiation detected) (Diehl et al. 2018).

4. Data Analysis Methods

The data used for this analysis is obtained by SPI operating in the 20 keV to 8 MeV energy range. However, instrumental background (BG) photons dominate the γ-ray spectra, which are of interest to answer the question of whether the Crab Nebula is a standard candle. The BG photons originate mainly from nuclear de-excitation reactions and continuum processes of the instrument and satellite material due to exposure to cosmic-rays. Therefore, to analyze the data provided by SPI a background model is necessary to distinguish the illumination patterns on the 19-element germanium detector array from BG and the source of interest (sky). To do this a maximum likelihood framework is used in the data analysis (Siegert et al. 2019). With the OSA software used for the standard analysis of SPI data, a two-step method is applied. First, only the photo peak response is used to incorporate the mask pattern on the detectors, and, second, an energy redistribution correction response is applied (Biltzinger et al. 2022). During this two steps statistical methods are used, which will be explained in Section 4.2. First the *Maximum Likelihood Estimation* (MLE) is used for the spectral extraction and afterwards either MLE again or a method based on *Bayesian Statistics* is used for the spectral fitting. The exact pipeline, consisting of several scripts within the OSA software (Courvoisier et al. 2003), used for the technical implementation of the statistical methods, will be described later on in Section 4.3.

4.1. Background Modelling

The data obtained from SPI comes in observation units, called *pointings* and a generic pointing is denoted with p. These pointings describe the measurement of SPI for a specific amount of time (typically 0.5 h to 1 h) and a specific region in the sky (Siegert et al. 2019) as explained in Section 3.2. Although, these data contain the X- and γ-ray spectra, they are dominated by BG photons. As the spectrum is not constant a subtraction of sources of interference is not applicable. Due to the unpredictable solar activity, a prediction model is not adequate to construct a usable background model either. Therefore the aim is to obtain a description of the BG directly from the data without taking the celestial source of interest into account (Siegert et al. 2019). A model about the data generation is used to provide a solution for the problem. Siegert et al. (2019) describe such a model and in the following a simplified version is presented. Accordingly, the data is generated through a function, mapping each pointing p into a model m_p characterized by the parameters θ and ψ. This function is

$$m_p(\theta, \psi) = \theta \cdot R_{SKY}(p) + \psi \cdot R_{BG}, \tag{10}$$

where R_{SKY} is the sky response, which is typically determined through particle physics simulations and cross-checked with calibrations on Earth. R_{BG} represents the background response which is initially unknown and has to be extracted from the data themselves. Notably, R_{SKY} can depend on p (and therefore it is a function), whereas R_{BG} is assumed to be independent of p. ψ is a multiplicative factor determining the number of photons in each detector. Finally, θ contains information about the flux F in units of counts $\mathrm{cm}^{-2}\,\mathrm{s}^{-1}$. Thus, θ is the variable of interest for the analysis. To obtain the desired parameter values statistical methods and numerical algorithms are applied.

4.2. Statistical Fitting Methods

To extract information out of a set of data a fit to a certain model is commonly used. As the data are often too complex for simple functions like a polynomial or a Gaussian function to fit well, the usual approach is to create a function depending on various parameters from an underlying theory expected to fit the given data. The parameters are specified to a value which fits best to the data. Hence, for a given predetermined model the adjustment process can be carried out by different optimization methods.

4.2.1. Maximum Likelihood Method

In general counting experiments, such as here for photons, follow a *Poisson distribution* with probability mass function (Siegert et al. 2019; Press et al. 1992):

$$P(D|\theta,\psi) = \frac{m_p(\theta,\psi)^{d_p} e^{-m_p(\theta,\psi)}}{d_p!}, \tag{11}$$

where $m_p(\theta,\psi)$ is the model with parameters θ and ψ as described in equation (10) to be fitted to the data set D. D consists of the number of photons d_p per pointing p. A likelihood $\mathcal{L}(D|\theta,\psi)$ gives the probability of measuring the entire data D, under the assumption that the model is governed by the parameters θ and ψ. Supposing independent draws across pointings, the likelihood $\mathcal{L}(D|m)$ is derived from equation (10) as the product of $N < \infty$, the total number of pointings in an measurement for a certain target source, probabilities $P(D|\theta,\psi)$ with $D = \{d_1, ..., d_N\}$ elements (Siegert et al. 2019):

$$\mathcal{L}(D|\theta,\psi) = \prod_{p=1}^{N} \frac{m_p(\theta,\psi)^{d_p} e^{-m_p(\theta,\psi)}}{d_p!}. \tag{12}$$

The MLE stipulates to search across all possible parameter values θ and ψ to maximize the likelihood $\mathcal{L}(D|\theta,\psi)$ of the observed data D given by equation (12). That is, intuitively speaking, MLE finds the model that fits the data the best (Siegert et al. 2019; Press et al. 1992). For calculation purposes, it is easier to work with the log-likelihood function henceforth, which does not alter the extrema of the original likelihood function because of the monotonicity of the logarithm:

$$\ln \mathcal{L}(D|\theta,\psi) = \sum_{p=1}^{N} \left(d_p \ln m_p(\theta,\psi) - m_p(\theta,\psi) - \ln d_p! \right). \tag{13}$$

At the maximum the partial derivatives with respect to both parameters have to be zero. These conditions allow to find the parameters which maximize the likelihood.

$$\begin{aligned}\frac{\partial}{\partial\theta}\ln\mathcal{L}(D|\theta,\psi) =& \frac{\partial}{\partial\theta}\sum_{p=1}^{N}\left(d_p\ln m_p(\theta,\psi) - m_p(\theta,\psi) - \ln d_p!\right) && (14)\\ =& \sum_{p=1}^{N}\left(\frac{d_p}{m_p(\theta,\psi)} - 1\right)\frac{\partial m_p(\theta,\psi)}{\partial\theta} && (15)\\ =& \sum_{p=1}^{N}\left(\frac{d_p}{m_p(\theta,\psi)} - 1\right)R_{SKY}(p) \overset{!}{=} 0. && (16)\end{aligned}$$

$$\begin{aligned}\frac{\partial}{\partial\psi}\ln\mathcal{L}(D|\theta,\psi) =& \frac{\partial}{\partial\psi}\sum_{p=1}^{N}\left(d_p\ln m_p(\theta,\psi) - m_p(\theta,\psi) - \ln d_p!\right) && (17)\\ =& \sum_{p=1}^{N}\left(\frac{d_p}{m_p(\theta,\psi)} - 1\right)\frac{\partial m_p(\theta,\psi)}{\partial\psi} && (18)\\ =& \sum_{p=1}^{N}\left(\frac{d_p}{m_p(\theta,\psi)} - 1\right)R_{BG} \overset{!}{=} 0. && (19)\end{aligned}$$

The last equation (19) can be simplified in case $R_{BG} \neq 0$. Then $\sum_{p=1}^{N}\frac{d_p}{m_p(\theta,\psi)} = N$. In either case numerical methods are used to solve for parameter values θ and ψ that satisfy equation (16) and (19). However, this method described only provides necessary conditions for a maximum and therefore sufficient conditions, like verifying the definiteness of the Hessian matrix, should be checked as well. Nevertheless, this step is skipped in this thesis. Similarly the software used will produce standard deviations for the parameter values, but the details are left out of this thesis.

4.2.2. Bayesian Statistics

To understand *Bayesian statistics* and the difference to *Maximum Likelihood statistics* first the concept of a prior has to be explained. The basic idea here is to include information which is already known or assumed (*a priori*) to get a 'weighted' estimate dependant on the prior belief and measurements. This means having a likelihood of the posterior probability containing the prior knowledge (prior probability) (Scargle 1998). For this purpose *Bayes' Theorem* plays a critical role:

$$P(M|D) = \frac{P(D|M)P(M)}{P(D)}. \tag{20}$$

The conditional probability $P(M|D)$ expresses the probability that M occurs, given that D is true and on the other way round $P(D|M)$ depicts the probability that D occurs, given that M is true. $P(M)$ and $P(D)$ describe the probability that M or D occur separately.

Bayesian statistics uses the likelihood $P(D|\theta, \psi)$ from Section 4.2.1 together with Bayes' Theorem. Furthermore, the prior $P(\theta, \psi)$ is part of the assumption and describes, without relying on the data, the distributions of the parameter values θ and ψ. $P(D)$ is the so-called *evidence*, a factor which is normally determined with algorithms like the *Markov Chain Monte Carlo* (MCMC) algorithm, but for the purposes here the evidence does not play a major role. Finally, $P(\theta, \psi|D)$ is the posterior distribution obtained from the objects above via Bayes' Theorem. Similarly to MLE, the model parameters that fit the data D best, according to this Bayesian approach, are obtained by maximizing the posterior likelihood, i.e. the posterior $P(\theta, \psi|D)$, by choice of θ and ψ :

$$\max_{\theta,\psi} \ln P(D|\theta, \psi) + \ln P(\theta, \psi). \tag{21}$$

Here, like in the MLE, a logarithmic transformation is applied to the objective and the constant term, i.e. the evidence, is dropped (Scargle 1998). For the *Bayesian Fit* the whole posterior distribution, across all parameter values, is calculated numerically, which also provides measures of parameters' uncertainties, like standard deviations, automatically.

4.3. SPI analysis pipeline

Several scripts within the OSA software are used to analyze the data of INTEGRAL:

4.3.1. Data selection

The first step of the data analysis is carried out using the software package *spiselectscw* written by Halloin (2009). With *spiselectscw* one can apply several data selection criteria, e.g. the time of the measurement of SPI (either the revolution or the science window—a $\sim$30 min time period consisting out of constant pointings), the selection on the sky direction (typically the angular distance between the pointing direction and the position of the object of interest), or the binning of the energy (Petry et al. 2009; Biltzinger et al. 2022). For my analysis the selection of the revolutions containing the Crab and the energy bins are of importance.

4.3.2. Background modelling

IDL background is a script written in the *Interactive Data Language* (IDL) and applied to build the background model to the time frame (revolution, science windows) data selected by spiselctscw.

4.3.3. Spectral extraction

Spimodfit is a script to perform model fitting with SPI data and is mainly used for the study of long duration observations and large scale emission. Here, the photo-peak response of the detectors is extracted, which depends on the source position to, e.g., take the absorption by the mask into account. In this first step, a photon flux F is fitted individually per energy channel with the model provided by equation (10) using the responses and the measured data in the individual SPI detectors, also considering the different background rates. This interim result is only a pseudo photon flux in units of counts $\mathrm{s}^{-1}\,\mathrm{keV}^{-1}$, because the energy dispersion and the detector energy resolution have not yet been accounted for. As explained above in Section 4.2.1, a MLE is used to fit the raw data in form of binned counts to multi component models taking the full instrument response function to estimate the parameters. For the calculation of the MLE a Levenberg-Marquardt algorithm is executed. Moreover, to accurately evaluate the uncertainties the Hessian matrix is inverted to calculate those from it (Halloin 2009; Biltzinger et al. 2022).

4.3.4. Spectral fitting

The *Multi-Mission Maximum Likelihood Framework* (3ML) is a python package programmed by Vianello et al. (2021). 3ML is utilized for an easy, coherent and intuitive modeling of sources using all available data independent of their origin. After the first step in the spectral extraction, in this second step the pseudo photon flux data points received by spimodfit are fitted with a spectral photon flux model and a correction response. This correction response depends on the energy bins used and should account for energy dispersion. It is impossible to incorporate energy dispersion to fit all energy channels individually. Therefore, all energy channels are fitted simultaneously, resulting in the steps between the different energy ranges visible in the spectra shown in figures in Section 5. Furthermore, this procedure leads to the flux to be given in units of counts $\mathrm{cm}^{-2}\,\mathrm{s}^{-1}\,\mathrm{keV}^{-1}$, which is the standard unit all flux values in the spectra in the following evaluation are presented by. The usage of 3ML takes place in 3 steps. First, one or more data sets are loaded and listed in a DataList object. Secondly, a model is defined, which contains a PointSource and a spectral function. Lastly, the fitting is executed to create the spectrum of the source data. This fitting can be done in

3ML either with the MLE or with Bayesian statistics as discussed in Section 4.2. For the MLE, 3ML includes methods, like *minuit* or *migrad*, to determine the maximum likelihood (cf. equation (12)). For Bayesian Fits a MCMC based integrator, e.g. in my case *emcee*, which is already implemented in 3ML, is used to infer the entire posterior distribution (Vianello et al. 2021; Biltzinger et al. 2022).

5. Evaluation

As mentioned above, to answer the main question of this thesis a current light curve of the Crab Nebula with data from the start of the mission up to the latest available data is constructed. Furthermore, a full spectral analysis of the whole Crab spectrum in the observation time is conducted.

5.1. Measured Data from 2003 - 2018

5.1.1. Data Selection

The data of the Crab measured by SPI have been separated in three different energy bands, because the different peculiarities of the SPI electronics chain have to be taken into consideration: SE (single-event, 20 keV to $\sim$ 600 keV), PSD (pulse-shape discriminated event range, $\sim$ 20 keV to 2000 keV), and HE (high-energy, 2000 keV to 8000 keV). For the data analysis of the Crab, data from all revolutions from the 19-02-2003 (revolution 43) to 14-10-2018 (revolution 2010), where the Crab has been visible at least in one science window, have been taken into account. Because the background model for the HE range has to be constructed with care as it is more influenced by the solar activity, the data analysis is restricted to the years 2003–2018. In the comparison to Jourdain and Roques (2020) (see Section 6.2.2), I used all the data available up to 12-09-2019 (revolution 2135) for the energy range 24–2000 keV, which does not need the HE energy range. Some further revolutions (explicitly, revolution 103, 170, 412, 1504, 1506, and 1715) have been left out of the data, because not enough information of the Crab was contained in the data or the flux values received were off in the scale of orders of magnitude. This lead to a total of 126 revolutions, which have been taken into account for the construction of the light curves and the spectral analysis. Furthermore, I only considered fluxes in the 24–50 keV band that show a significance of more than 85 standard deviations, henceforth just σ. Data with smaller significance were neglected. The value 85 has been chosen because we want to see flux variations on the order of 1% being undisturbed by statistical fluctuations of the measured values assuming an underlying normal distribution.

For the individual analysis of each revolution a binning of 0.5 keV, 5 keV, and 100 keV for the SE, PSD, and HE energy bands respectively was set to improve the quality of the fit and reduce the uncertainties. For the total spectrum over all revolutions a logarithmic binning was used due to computational limitations.

5.1.2. Application of the Methods from Section 4

First, to get all revolutions from INTEGRAL containing the Crab, I extracted the data from the *INTEGRAL Science Data Centre* (2022) and programmed a script to select all revolutions. To generate the light curve and perform the spectral analysis the scripts described in Section 4.3 have been executed for every individual revolution which included the Crab. Therefore, I have written an automatic program, which inserts the revolutions as a parameter and executes the pipeline described in Section 4.3 for all revolutions. Furthermore, with the usage of the python package 3ML (see Section 4.3.4) a *Maximum Likelihood Fit* as described in Section 4.2.1 with a broken power-law with fixed break-energy at $x_b = 100\,\mathrm{keV}$ was carried out for each revolution to fit spectra and obtain spectral parameters. Also, I used 3ML to fit different models to the total spectrum using Bayesian Statistics as shown in Section 5.3.2.

5.2. Construction of the light curves

The best method to validate the variability of the Crab flux evolution is to inspect the source flux against the time, given in Modified Julian Days (MJD), which leads to a light curve. In my analysis, I made several light curves showing the Crab emission since 2002 until 2018 with different methods mentioned before. The light curves for the energy bands 24–50 keV and 50–150 keV with the data received after the fitting with 3ML using MLE are shown in Figure 10. Further light curves for higher energy bands and different data extraction methods can be found in the appendix A.1. It appears that the Crab is varying around a stable mean flux marked as the blue dash-dotted line. Except for some outliers, most points are contained within a 5% deviation around the mean flux in the 24–50 keV and 50–150 keV energy band shown as the cyan dash-dotted lines. These outlier points might be explained through a fit with a low goodness of fit value in the spimodfit process. While the Crab seems to vary rapidly from 2002 to 2012 and no definite evolution is clearly observable, a decrease is visible from 2015 to $\sim$ 2017 with a starting increase again afterwards. Also from 2008 to 2010 a decrease is noticeable—even though not as salient—which matches with the results from Wilson-Hodge et al. (2011) (see Section 6.1). Whilst the variation of about $\sim$ 5% is present for the energy range 24–150 keV, the Crab emission fluctuates much more in the higher energy bands 150–400 keV and 400–650 keV Figure 21 (see appendix A.1) and especially for 650–2000 keV and 2–8 MeV in Figure 22 (appendix A.1). It is debatable if the Crab evolution trends seen in the two low-energy bands are still visible in the 150–400 keV band, but there is manifestly no certain trend noticeable for higher energy bands.

In addition to the light curves made from the results after the 3ML spectral fitting, I also constructed light curves directly with the flux results given by spimodfit. These can be seen in Figure 11 for the low energy bands (24–150 keV) and in the appendix A.1 for the higher energy bands (Figure 23 and 24 for 150–650 keV and 650–8000 keV, respectively). Except for the flux value and unit, the low energy light curves (Figure 11) look mostly similar to the 3ML low energy light curves (Figure 10). For the higher energy bands first of all significantly greater error bars are visible. These probably come from the spectral extraction in spimodfit, resulting in larger uncertainties after the maximum likelihood estimation. Due to the spectral fitting with 3ML, the uncertainties flatten out over the bin width and consequently decrease in size. Furthermore, this significant flux variations in the high energy domain lead to possible fluxes with negative value, which would be void of any physical interpretation. However, due to the large uncertainties it cannot be rejected that these values are zero or even strictly positive, except for very few outliers in the 2000–8000 keV energy band.

Lastly, I applied the method of *Bayesian Blocks* after Scargle (1998) with the Python package *astropy* to the 3ML light curves. *Bayesian Blocks* build up on *Bayesian statistics* and specify an algorithm to characterize intensity variations. Here, an output is generated, which describes the most probable segmentation of the observation into time intervals during which the photon arrival rate is perceptibly constant, i.e., has no statistically significant variations (Scargle 1998). With a certain threshold applied, this leads to a redistribution of the analyzed revolutions into larger groups: 43–53, 54–123, 124–203, 204–512, 513–635, 636–751, 752–804, 805–837, 838–870, 871–994, 995–1020, 1021–1025, 1026–1058, 1059–1092, 1093–1217, 1218–1302, 1303–1491, 1492–1621, 1622–1861, 1862–1872, 1873–2010. With this new categorization, I executed a new analysis with the OSA software. Due to computational reasons a logarithmic binning was used, instead of the 0.5 keV, 5 keV, 100 keV for the SE, PSD, and HE spectra, respectively. The new evaluation resulted in the 3ML MLE light curves which are displayed in Figure 12 (24–150 keV) and in the appendix for the higher energy bands (Figure 25 and Figure 26 for 150–650 keV and 650–8000 keV, respectively). However, the method did not improve the variability of the Crab flux in the low-energy bands (Figure 12) compared to the original 3ML light curve (Figure 10). It seems though, that the trends of the Crab evolution are more clearly visible now, especially the decline between 2008 and 2010 reported by Wilson-Hodge et al. (2011). Moreover, the variability of the Crab flux in the high energy segment (cf. appendix A.1, Figure 25 and 26) is less than in the initial 3ML light curves (cf. appendix A.1, Figure 21 and 22) and the error bars are smaller.

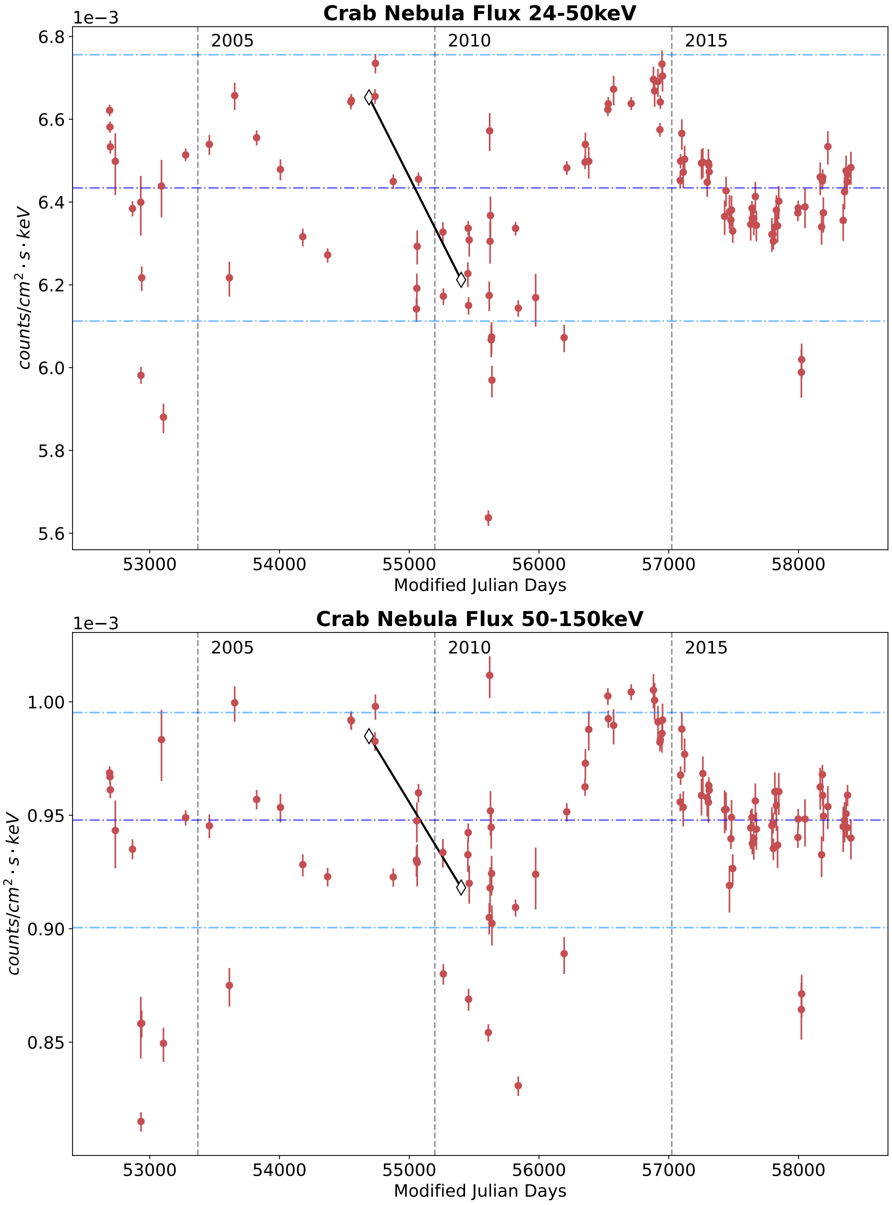

Figure 10: Light curves of the Crab emission from the start of the mission until October 2018. Each red point corresponds to one revolution of INTEGRAL (∼ 0.5 to 2.5 days of useful duration) where the Crab was measured. The flux data was retrieved from the spectral fit data from 3ML. The blue dotted-dashed line represents the weighted mean flux value, the cyan dotted-dashed lines represent the ±5% tolerance around it. The gray vertical dashed lines represent the start of the year shown at the top right of the lines. The black lines picture the source decline reported by Wilson-Hodge et al. (2011) from MJD 54690 to MJD ∼ 55400 with a total slope of ∼ 7%. Top: Light curve in the 24–50 keV range. Bottom: Light curve in the 50–150 keV range.

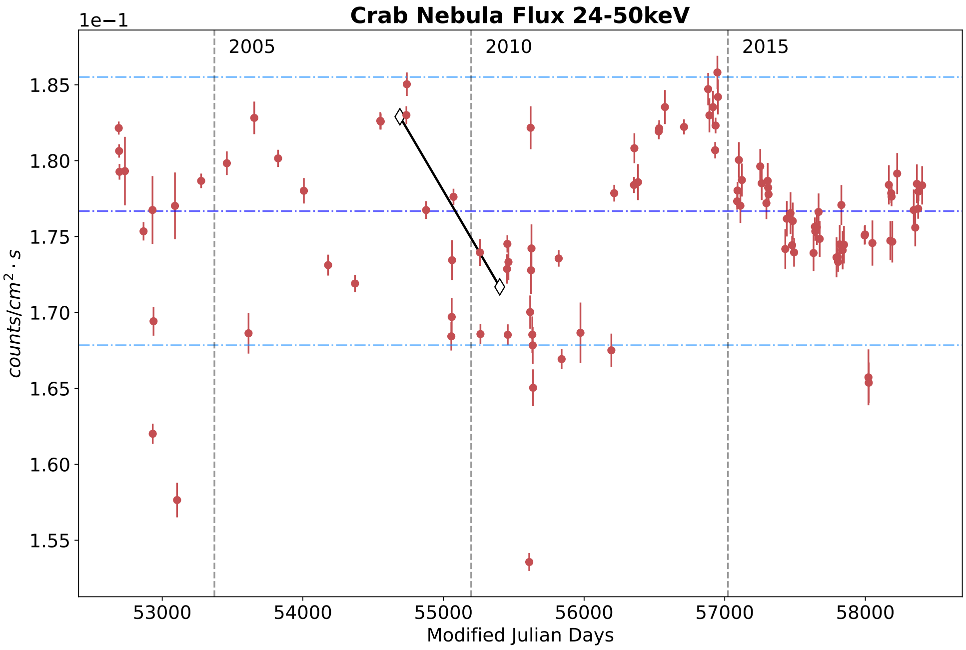

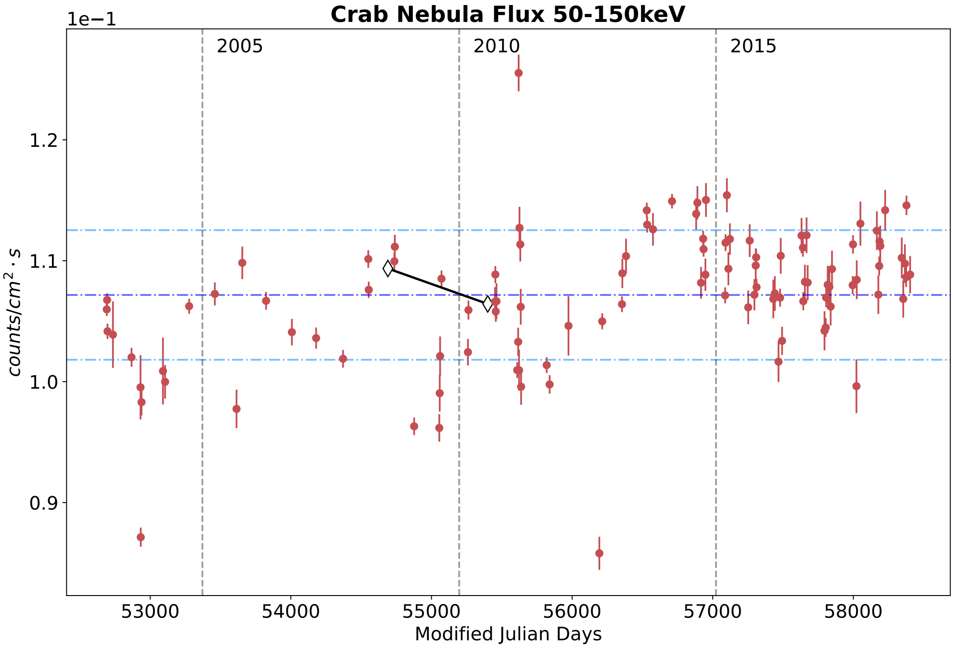

Figure 11: Similar to the description from Figure 10, but here the flux data per revolution has been retrieved directly from the spimodfit result instead of after the 3ML spectral fitting. The black lines picture the source decline reported by Wilson-Hodge et al. (2011) from MJD 54690 to MJD $\sim$ 55400 with a total slope of $\sim$ 6.1% (top) and $\sim$ 2.7% (bottom).

Nevertheless, a direction of the Crab evolution is still not distinctly visible for the high energy bands.

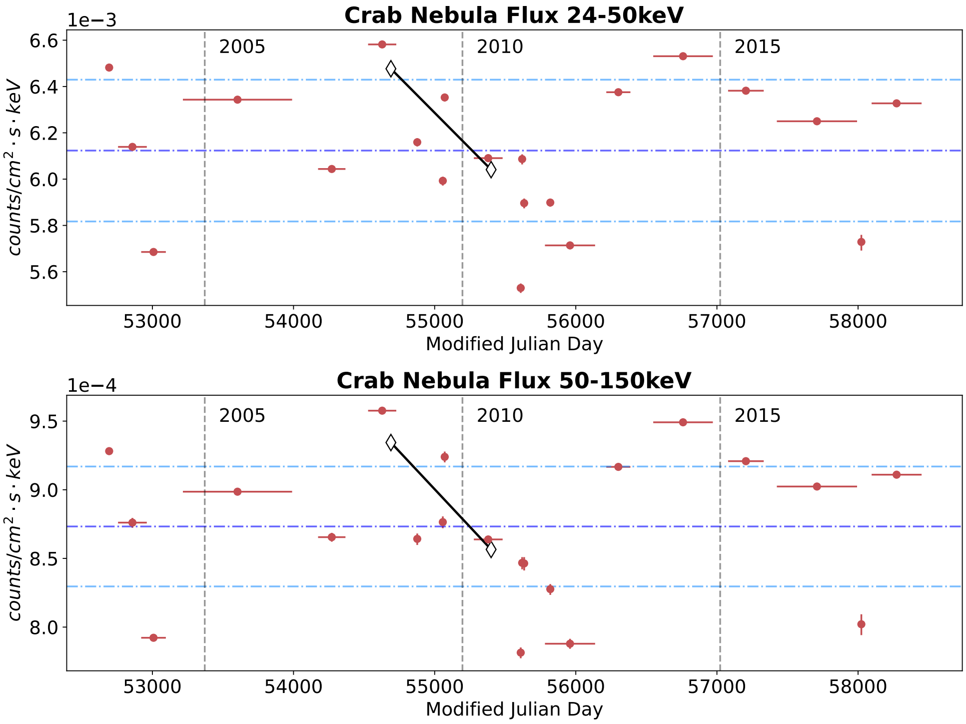

Figure 12: Similar to the description from Figure 10. Here data points with similar flux value have been merged together through the usage of the Bayesian blocks method and a separate data analysis with the INTEGRAL OSA software for the combined revolutions has been executed. Hence, a red data point represents the average flux value over the whole time frame of the x-error bar. The black lines picture the source decline reported by Wilson-Hodge et al. (2011) from MJD 54690 to MJD $\sim$ 55400 with a total slope of $\sim$ 6.7% (top) and $\sim$ 8.3% (bottom).

5.3. Spectral Analysis

The energy spectrum of the Crab has been described by a power-law for most of the energy domains covered by individual instruments for a long time. In the last $\sim$ 15 years new observations indicated a more complex spectral shape and new models like a broken power-law or the Band Model were tested (Jourdain and Roques 2020). First, I take a look at the individual spectra per revolution. Afterwards I will discuss the combined spectrum of the Crab from revolution 43 to 2010 and different fitting models. Further on, a discussion of the variability of the fit parameters follows.

5.3.1. Individual Spectrum per Revolution

For all 126 analyzed revolutions, I used a broken power-law with a break-energy at $x_b = 100\,\mathrm{keV}$ to describe the slope evolution of the individual spectra. The formula of a broken power-law is given by following equation:

$$f(x) = K \begin{cases} \left(\frac{x}{x_b}\right)^{\alpha} & x < x_b \\ \left(\frac{x}{x_b}\right)^{\beta} & x \geq x_b \end{cases}, \tag{22}$$

with α and β describing the low- and high-energy slope separated by the break-energy x_b, respectively, and x in this case being the energy. K represents the normalization value at the break-energy x_b. Figure 13 shows an exemplary result, here for revolution 43 made with a maximum likelihood fit in 3ML. The SE, PSD, and HE spectra were fit together using the same shape parameters. To reduce the uncertainties and improve the quality of the fit, I used the smallest public available bin size in SPI data analysis of 0.5 keV (Siegert et al. 2019) for the whole SE spectrum from 24–600 keV. For the PSD spectrum, a 5 keV binning, and for the HE spectrum a 100 keV binning was applied throughout. The energy range from 20–24 keV has been left out due to large residuals. However, for the remaining spectra up to 8 MeV nearly all residuals lie within 4σ, most even within 2σ, suggesting a good fit of the broken power-law. Nevertheless one can notice, that in the HE spectrum more data points lie above the fitted spectrum. For this reason, besides the broken power-law, I will consider two different spectral models in the following section.

5.3.2. Mean Spectrum

Next, I analyze the mean spectrum across all measured revolutions (43–2010). Additionally to the broken power-law with a fixed break energy at 100 keV used for the individual spectra, I evaluate two further models to describe the slope evolution of the Crab spectra for better results. Furthermore, instead of a maximum likelihood method, Bayesian statistics were used in 3ML for the spectral fitting. The Bayesian approach allows me to set the priors of the fit parameters to a distribution expected from the results in Section 5.3.1 above. As for small energies below 50 keV extreme results in regards to the residuals were present in all three models for the mean Crab spectra, the energy range from 20–50 keV was disregarded.

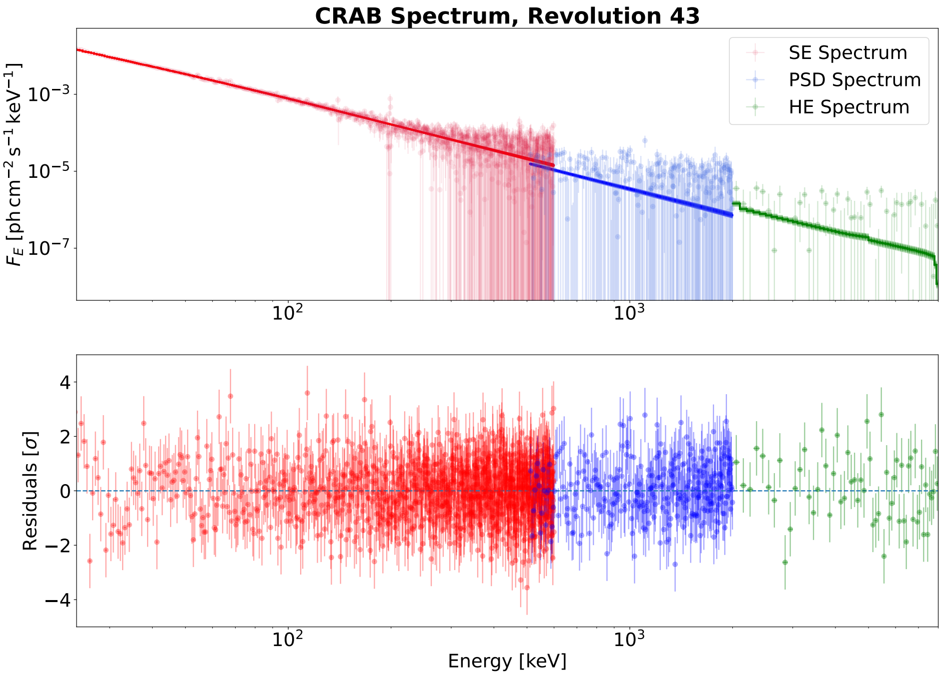

Figure 13: Top: Spectrum of the Crab, here for example in revolution 43, starting at 24 keV until 8000 keV against the flux F_E. A broken power-law with a break-energy at $x_b = 100$ keV was used to fit the data. The different photon events (SE, PSD, HE) measured are shown in different colors. Bottom: Residuals of the data points to the fit in terms of σ. A data point corresponds to one energy bin.

First, after the fit with the broken power-law, a fit with the Band model as proposed by Jourdain and Roques (2020), was used. 3ML uses the following Band function;

$$f(x) = K \begin{cases} \left(\frac{x}{piv}\right)^{\alpha} \exp\left(-\frac{(2+\alpha)x}{x_b}\right) & x \leq (\alpha-\beta)\frac{x_b}{(\alpha+2)} \\ \left(\frac{x}{piv}\right)^{\beta} \exp(\beta-\alpha)\left[-\frac{(\alpha-\beta)x_b}{piv(2+\alpha)}\right]^{\alpha-\beta} & x > (\alpha-\beta)\frac{x_b}{(\alpha+2)} \end{cases}, \tag{23}$$

with α and β being the low- and high-energy slope separated by the break-energy x_b, respectively. K indicates the normalization value at the pivot energy (piv), which has been fixed to $piv = 100$ keV. However, with the data at hand the fit did not converge, if the lower bound of the priors' support for the break-energy x_b in the Bayesian analysis was set above 50 keV. In comparison Jourdain and Roques (2020) reported a break-energy around ∼530 keV with the Band Model; (more in Section 6.2.2). Consequently, a break-energy of 50 keV results in a meaningless value of the low energy slope index α, because the analysis of the spectra first starts at 50 keV and therewith α having no effect on the data. Fixing the break-energy at 530 keV resulted in the same problem of the fit not converging. Moreover, the normalization value appears to be inconsistent (see Table 1). This might be explained as a scaling issue caused by the pivot energy set to 100 keV. Thus, the band model was not put into further consideration, as the broken power-law (equation (22)) with one break-energy at 100 keV provides better results for the mean spectra.

Secondly, as for the individual spectra more data points were located above the fit in the HE range, a broken power-law with two break energies seems more appropriate than a broken power-law with one break-energy. For this the following formula was used to fit the spectra in 3ML:

$$f(x) = K \begin{cases} x^{\alpha} & x \leq x_{b1} \\ x_{b1}^{\alpha-\beta} x^{\beta} & x_{b1} \leq x \leq x_{b2} \\ x_{b1}^{\alpha-\beta} x_{b2}^{\beta-\gamma} x^{\gamma} & x_{b2} \leq x \end{cases}, \tag{24}$$

with α, β, and γ being the slopes before the break-energy x_{b1}, between the break-energies x_{b1} and x_{b2}, and after the break-energy x_{b2} respectively and K being the normalization at x_{b1}. The lower bound of the prior's support x_{b1} was set to at least 100 keV. Not fixing the first break-energy would result in an estimate of x_{b1} at approximately 50 keV causing the same problem as for the Band model, which in turn renders the α-parameter obsolete. Figure 14 displays the result from 3ML for the broken power-law with two break-energies.

To compare the three models, Table 1 reports the best-fit parameters. I used the *Akaike Information Criterion* (AIC) (Akaike 1974; Cavanaugh 1997) as an absolute figure-of-merit to determine a fit's quality. In general, a smaller AIC, suggests a better model fit (Siegert et al. 2019). Additionally, to better differentiate the three models, Figure 15 displays them in model space. There, the flux is multiplied by the energy squared and also marked with the dotted lines according to the same color as the model, which makes the break energies more salient. The different shades per color symbolize confidence intervals for different coverage probabilities (0%, 68.3%, 95.4%, 99.7%). The difference in the α-parameter for the band model compared to the other models below 50 keV is evident. Besides that, the influence of the high energy slope γ in the broken power-law model with two break energies is distinctly visible.

Even though there is no physical explanation for the second energy break at ∼300 keV yet, the new model with two break energies fits best to the Crab spectrum measured as

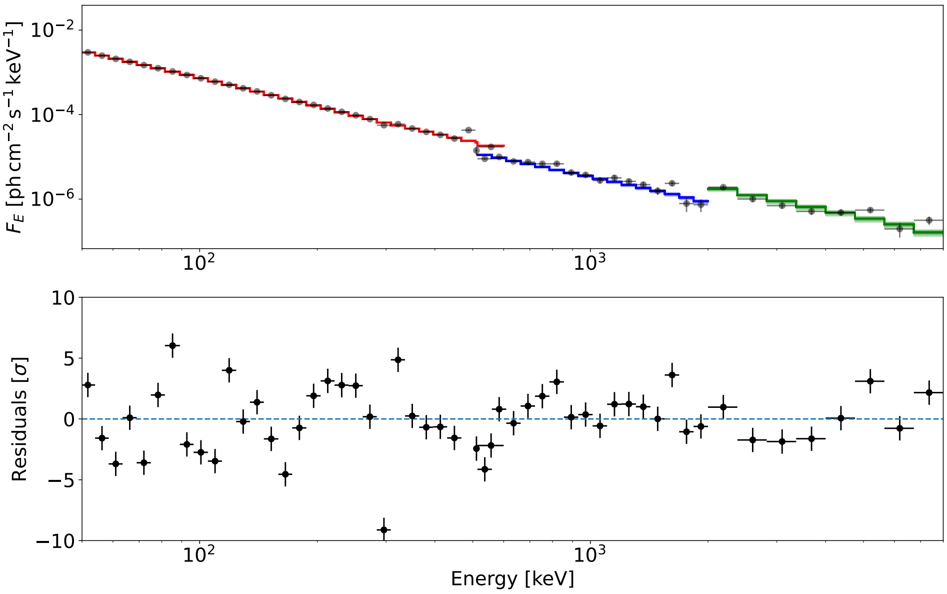

Figure 14: Top: Spectrum of the Crab from revolution 43 to 2010 starting at 50 keV until 8000 keV against the flux F_E. A broken power-law with two break energies ($x_{b1} = 100\,\text{keV}$, fixed, $x_{b2} = (302 \pm 6)\,\text{keV}$) is fitted to the data. The three different colors—red, blue, green—represent the different photon energies measured—SE, PSD, and HE, respectively. Bottom: Residuals of the data points to the fit in terms of σ. A data point corresponds to one energy bin.

seen in Figure 14 and from the AIC values in Table 1.

5.3.3. Variability of the Fit Parameters

To analyze the evolution of the spectral parameters with time, the best-fit parameters have been extracted for each individual revolution. As the break-energy was fixed to 100 keV for the broken power-law, I obtained the time series of the low-energy slope α and high-energy β over all revolutions used in the light curves. Figure 15 visualizes the results. The blue dash-dotted line again represents the weighted mean value, which result in $\alpha_{mean} = -2.08 \pm 0.03$ and $\beta_{mean} = -2.27 \pm 0.18$. Here, the uncertainty derives as one standard deviation of the weighted mean, which is marked as the cyan dash-dotted lines around the mean value. Both α as well as β are contained within 1σ for 76% and 73% of the data points, respectively. This roughly corresponds with the

Table 1: Crab Nebula best-fit parameters for the three models (broken power-law with one break-energy (BPL, x_{b1}, equation (22)), broken power-law with two break-energies (BPL, x_{b1} & $_{b2}$, equation (24)), Band Model (equation (23))) used to fit the mean spectrum for revolution 43-2010. The AIC-value describes the goodness of fit. Smaller AIC indicates a better fit.

	α /	x_{b1} [keV]	β /	x_{b2} [keV]	γ /	K [$\mathrm{cm^{-2}\,s^{-1}\,keV^{-1}}$]	AIC /
BPL, x_{b1}	-2.130 ± 0.003	100.7 ± 0.6	-2.210 ± 0.004	/	/	11.9 ± 0.2	419
BPL, x_{b1} & x_{b2}	-2.124 ± 0.003	100	-2.230 ± 0.004	301 ± 55	-1.89 ± 0.02	11.6 ± 0.2	588
Band Model	-1.71 ± 0.02	50.2 ± 0.2	-2.195 ± 0.004	/	/	$0.001\,14 \pm 0.000\,04$	612

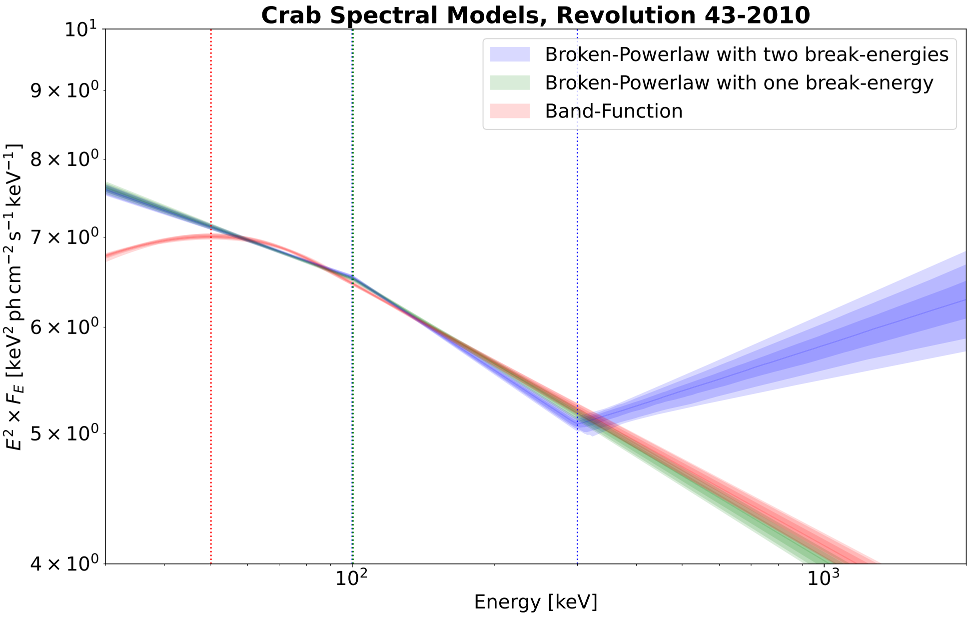

Figure 15: Shown are the different fitting models—broken power-law with two break-energies in blue; broken power-law with one break-energy in green; Band-Function in red—in model space. The dotted lines at 50 keV (red), ∼ 100 keV (green and blue), and ∼ 300 keV (blue) represent the break energies of the fitted functions with matching color. The flux has been multiplied with the energy squared for better visibility of the break-energies.

first confidence interval of the normal distribution of 68.3%, underlying the stability of the Crab emission in terms of shape.

On the other side, the de- and increases of the Crab flux seen in the light curves are not visible in the evolution of the best-fit parameters. This gets clear when plotting α (or β) against the flux. Figure 17 shows α against the two low energy bands (24–50 keV and 50–150 keV). The blue dash-dotted lines in Figure 17 represent the weighted mean value for α (vertical) and the Crab flux (horizontal). As expected, most points lie close to the intersection point of the two weighted means. Furthermore, Table 2 shows the correlation coefficients to quantify the interpretation from Figure 17. Only a small positive correlation for α and a small negative correlation for β between the best-fit parameters and the flux could be observed. Noteworthy, the correlation coefficient for α against the 50–150 keV is higher than the other correlation coefficients showing a clear positive correlation.

Table 2: Correlation coefficients of the low-energy slope α and high-energy slope β to the Crab flux for the two low-energy bands.

	α	β
Flux 24–50 keV	0.25	-0.20
Flux 50–150 keV	0.69	-0.26

Comparing the received weighted mean values with the slopes of the total spectrum from Revolution 43-2010 (see Table 1) a good agreement within the margin of error is noticeable, again emphasizing the stability of the Crab emission in over $\sim$ 15 years of measurement.

In addition, I analyze the evolution of the best-fit parameters for the spectra received after the new segmentation obtained from the *Bayesian Blocks* method (Scargle 1998) (see Section 5.2). Figure 18 displays the outcome. For the low-energy slope α a weighted mean value of -2.12 ± 0.02 and for the high-energy slope β a weighted mean value of -2.22 ± 0.03 was obtained. The uncertainties are given as one standard deviation of the weighted mean value. The result slightly differs from the result of the individual spectra in Figure 18, but still agrees within 1σ for α and 2σ for β. Additionally, it provides exactly the same values as the total spectrum with the broken power-law with one break-energy at 100 keV when compared to Table 1. This reassures that all points are consistent with each other.

Concluding it can be said, that the best-fit parameters of the low-energy slope α and high-energy slope β are well consistent in the evolution of the Crab emission, accentuating the Crab as a stable source in shape.

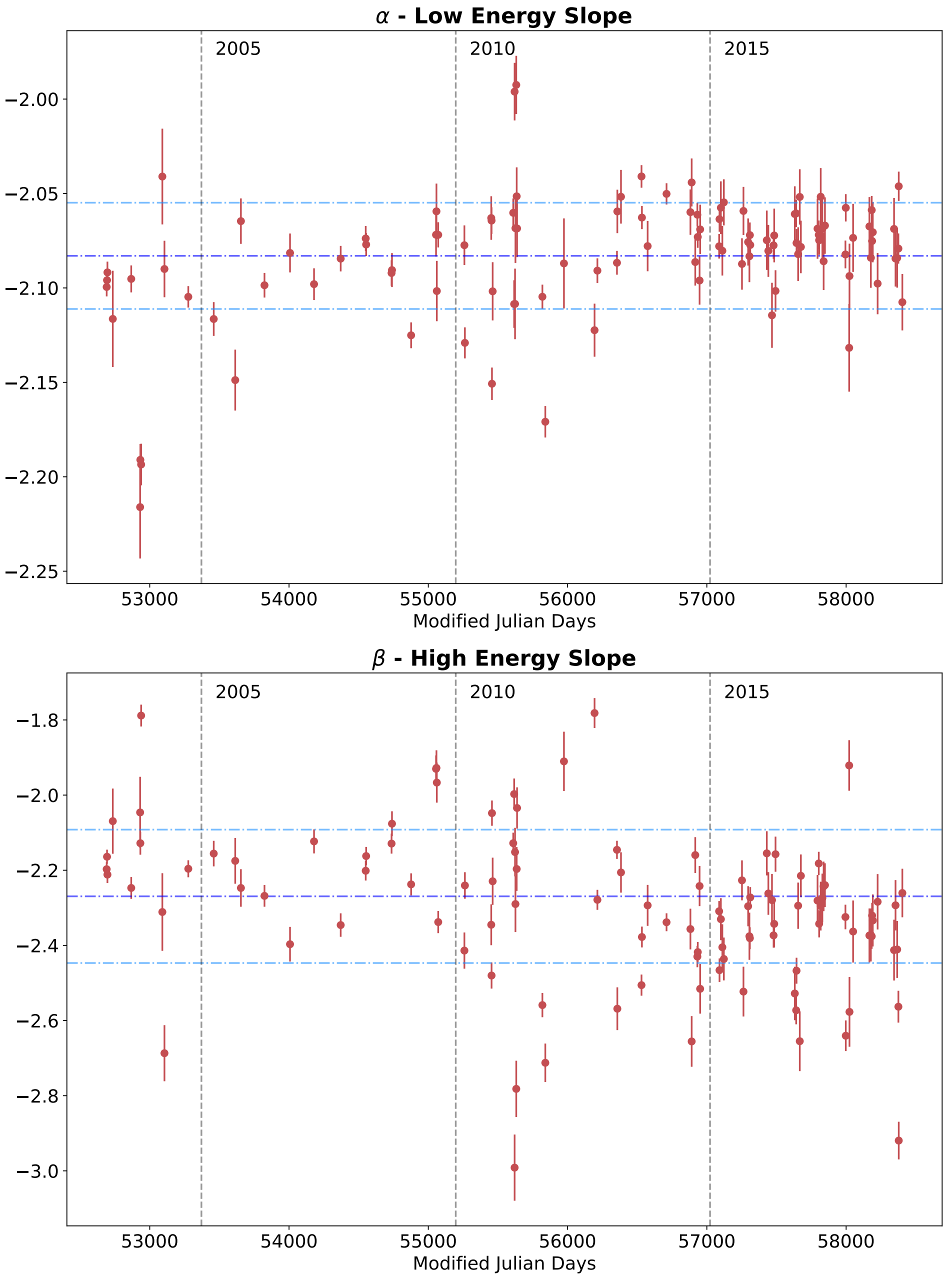

Figure 16: Best-fit parameter evolution for the low-energy slope α (top) and the high-energy slope β (bottom) from the fitted broken power-law via 3ML using MLE over time (Feb. 2003 to Oct. 2018). The break energy has been fixed to 100 keV. Each red point corresponds to one revolution of INTEGRAL where the Crab has been measured and a 3ML spectral fitting was executed. The blue dotted-dashed line represents the weighted mean value, the cyan dotted-dashed lines represent the 1σ confidence interval around it.

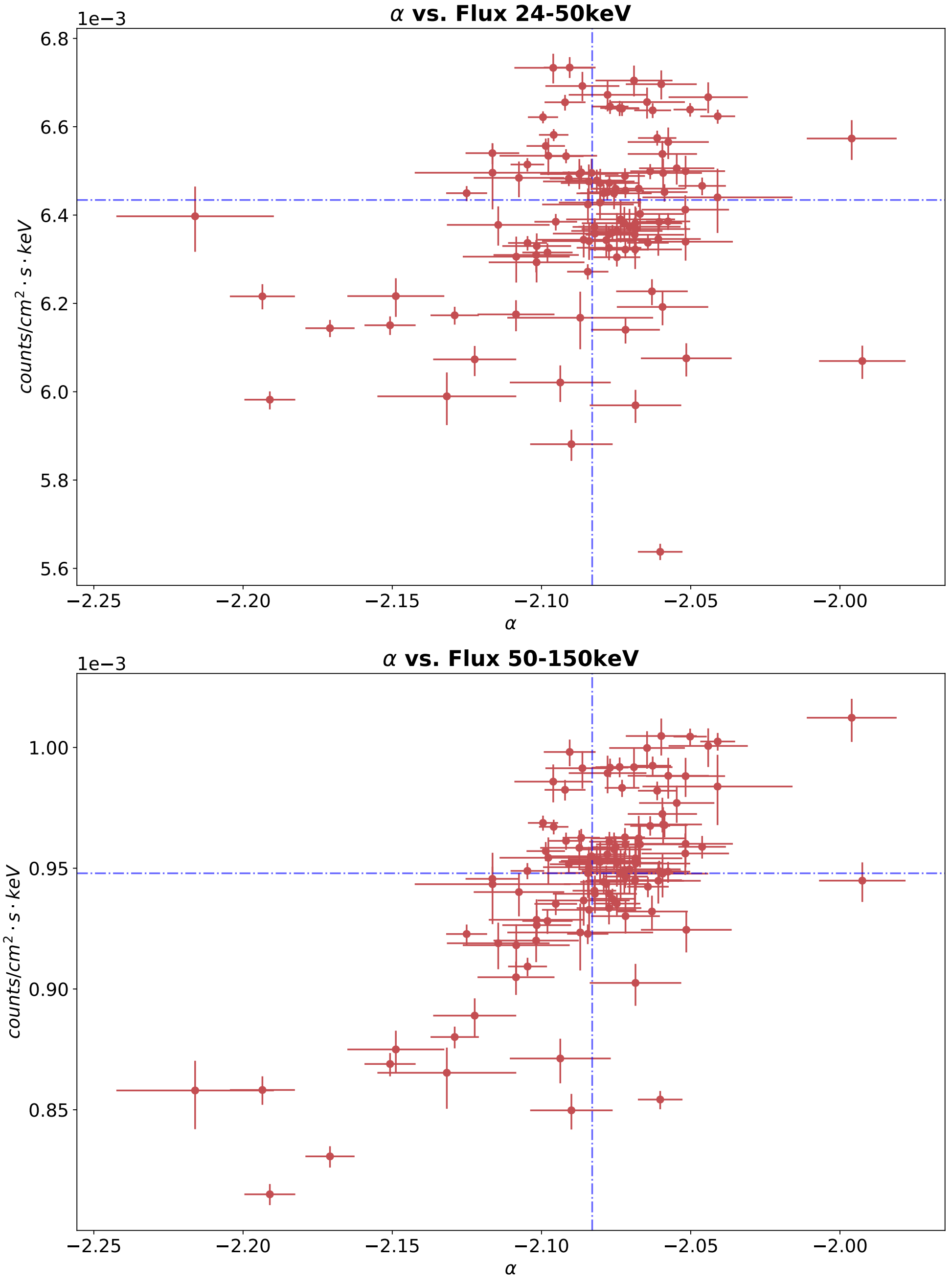

Figure 17: Low-energy slope α against the Crab flux for the two low energy bands (top: 24–50 keV, bottom: 50–150 keV). Each red data point corresponds to one revolution. The blue dash-dotted lines represent the weighted mean value of α (vertical) and the Crab flux (horizontal).

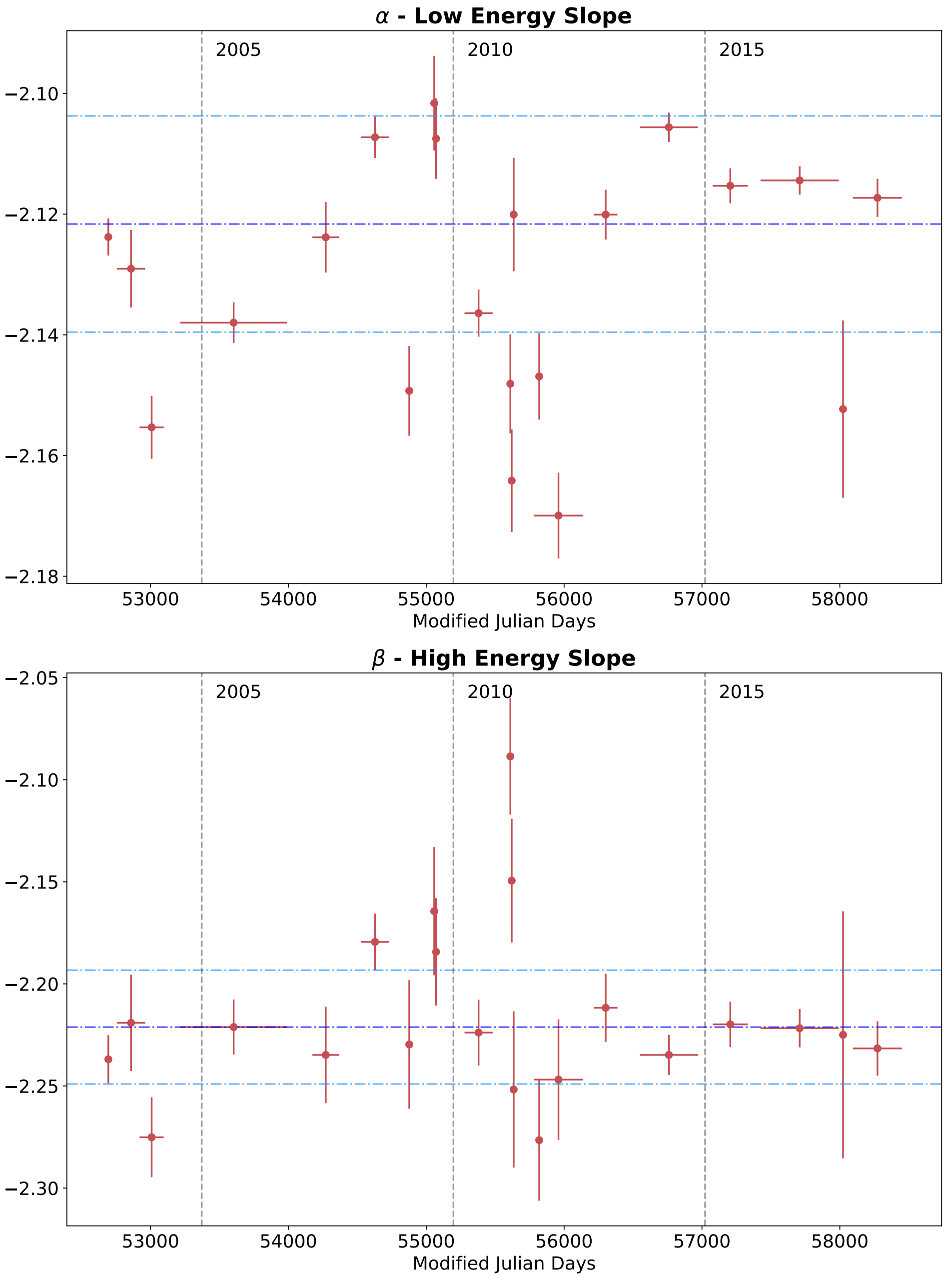

Figure 18: Similar to the description from Figure 16. Here data points with similar flux value have been merged together through the usage of the Bayesian blocks method and a separate data analysis with the INTEGRAL OSA software for the combined revolutions has been executed. Hence, a red data point represents the average flux value over the whole time frame, given by the corresponding horizontal error-bar.

6. Comparison to previous results

6.1. Comparison to the results from Wilson-Hodge et al. (2011)

Wilson-Hodge et al. (2011) reported an intrinsic variation of the Crab at a level of $\sim$3.5 %/yr. Furthermore, they registered a decline of the Crab flux of $\sim$ 7% for about two years starting at MJD 54690 (2008-2010) in the 15–50 keV and in the 50–100 keV band with several instruments including INTEGRAL/IBIS. In their study the *Fermi*/GBM instrument even measured a decline of (12 ± 2) % and (39 ± 13) % in the 100–300 keV and 300–500 keV energy range, respectively.
For better comparison, the decline observed by Wilson-Hodge et al. (2011) is marked in my resulting light curves with black lines from MJD 54690 to MJD 55400. However, this method might easily prone to uncertainties due to the non negligible strong short term variations in my light curves, especially for higher energies. Nevertheless, for the 3ML light curves (Figure 10 and 21) this method results in a percentage decline of the Crab flux starting at MJD 54690 of $\sim$ 6.6%, $\sim$ 6.8%, and $\sim$ 18% for the 24–50 keV, 50–150 keV, and 150–400 keV, respectively. For the spimodfit light curves (Figure 11 and 23) a percentage decline of the Crab flux starting at MJD 54690 of $\sim$ 6.1%, $\sim$ 2.7%, and $\sim$ 11% for the 24–50 keV, 50–150 keV, and 150–400 keV, respectively, can be seen. Especially the result for the 50–150 keV energy band is off with respect to the other energy bands and the result from Wilson-Hodge et al. (2011). Due to high residuals in the spimodfit spectral extraction, presumably due to high background variations, the points between MJD 54690 and 55400 are not reliable. For the light curves generated with the *Bayesian Blocks* method (Figure 12 and 25) my method leads to a percentage decline of the Crab flux starting at MJD 54690 of $\sim$ 6.7%, $\sim$ 8.3%, and $\sim$ 11% for the 24–50 keV, 50–150 keV, and 150–400 keV, respectively. In general it can be said, that the declines I obtain are compatible with the results from Wilson-Hodge et al. (2011), especially in the low-energy band 24–50 keV.

6.2. Comparison to the results from E. Jourdain & J. P. Roques

E. Jourdain and J. P. Roques specialized on the analysis of the Crab Nebula since many years. In the end, I want to compare my results with their findings from 2009 and 2020.

6.2.1. Comparison to Jourdain and Roques (2009)

In their analysis of SPI data Jourdain and Roques (2009) investigated the Crab emission for three long term spectra. They examined the spectra for revolution 43-45 (called sum1), revolution 239-605 (sum2), and revolution 665-727 (sum 3) and fitted a broken power-law with a fixed break-energy at 100 keV to each of them. To compare the results

I used their data (Table 1 and 2 from Jourdain and Roques (2009)) and plotted them in Figure 19. For better clarity I subdivided the spectra in four plots with different energy ranges. The data for sum1, sum2, and sum3 of Jourdain and Roques (2009) are shown as the purple data points, their broken power-law fits as the purple lines (as the fit-parameters are similar, the three lines overlap looking like a thick line). Furthermore, I added my mean spectra for revolution 43-2010 to the plot. My data are shown as the black dots and the fitted broken power-law with two break-energies (x_{b1} =100 keV and x_{b2} =$\sim$ 300 keV) are the 'stairs' (symbolizing the bin width) in the colors red, blue, and green for the SE, PSD, and HE energy range, respectively. One can see, that my data analysis matches well with Jourdain and Roques (2009). However, the flux values I calculated are always slightly higher than theirs. When comparing the models, the slopes look quite similar. This is validated when comparing the exact values. Jourdain and Roques (2009) report a low-energy slope α of ~ -2.05 and a high-energy slope β of ~ -2.25. For the broken power-law with two break-energies, I obtain $\alpha = -2.124 \pm 0.003$ and $\beta = -2.230 \pm 0.004$. Hence, my α-parameter is slightly higher than theirs, while β agrees within 5σ. Moreover, the difference in the models used is visible in the high energy plot (1600–8000 keV at the bottom right corner of Figure 19). Whilst their broken power-law fits fine also in the higher energy range, my data stays at higher flux rates, suggesting the second break-energy at $\sim$300 keV. In summary, my results coincide with Jourdain and Roques (2009) for the most part. The results show, that even though I used a different time frame than Jourdain and Roques (2009), the outcome is fairly similar, suggesting the stability of the Crab emission in shape.

6.2.2. Comparison to Jourdain and Roques (2020)

In their paper Jourdain and Roques (2020) did a full analysis of the Crab emission monitored by INTEGRAL SPI from 2003 to 2019. In the process they constructed a light curve of the Crab evolution, tested the spectra of the Crab for the individual revolutions and as two mean spectra and studied the variation of the best-fit parameters. For this, they divided their data in two time frames, first revolution 43-1196 (2003-2011) and secondly revolution 1214-2135 (2012-2019) and in four energy bands, 24–50 keV, 50–150 keV, 150–400 keV, and 400–650 keV.

First, I compare the light curves (Figure 1 in Jourdain and Roques (2020)). Jourdain and Roques (2020) used noticeably less revolutions and consequently their result shows no short term variations. They, however, show the same trend in the low-energy bands as seen in my light curves (see Figure 10): the decrease reported by Wilson-Hodge et al. (2011) from $\sim$ 2008 to 2010 and the decrease from $\sim$2015 to 2017. In the higher energy bands, especially starting at 400–650 keV, no clear trend is visible anymore.

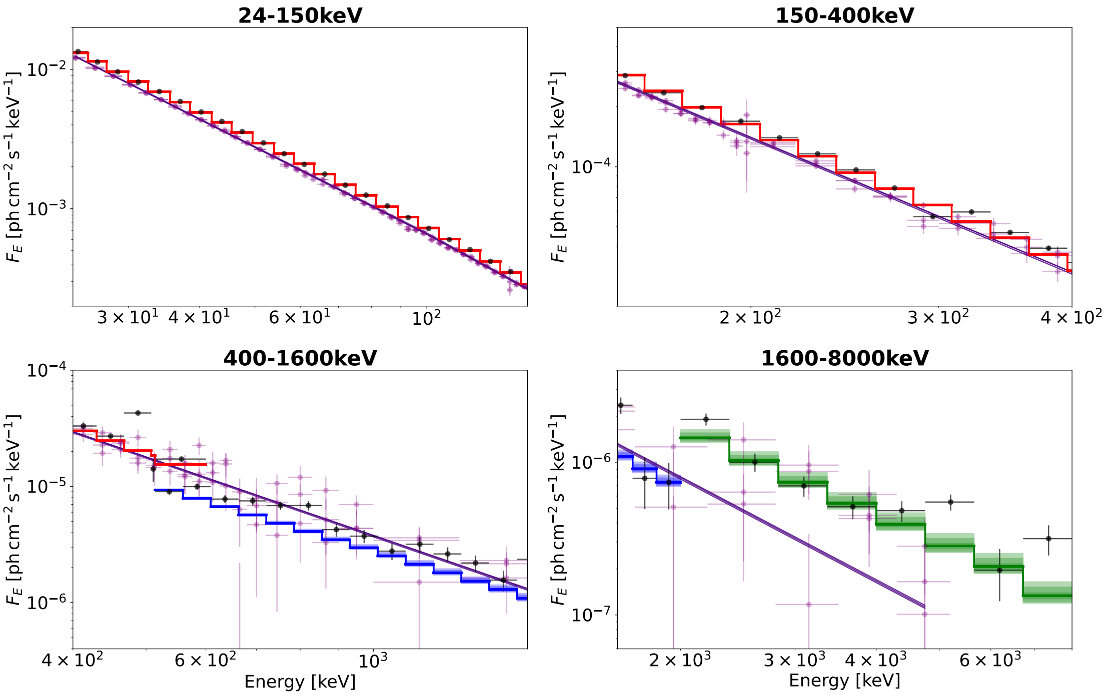

Figure 19: Jourdain and Roques (2009) examined three different time frames (revolution 43-45, rev. 239-605, and rev. 665-727) and fitted the spectra with a broken power-law model with a fixed break-energy at 100 keV. Their data is shown as the purple data points and lines. In comparison my total spectrum from revolution 43 to 2010 with a broken power-law with two break-energies at 100 keV and ∼300 keV is plotted on top of their data. My data points are marked as the black dots, and the fitting model in red, blue, and green color for the SE, PSD and HE range, respectively.

Furthermore, their flux value measured is always between 5% and 10% higher than the flux value I measured. For example in the 24–50 keV band their mean value lies at $\sim 6.8 \times 10^{-3}\,\mathrm{cm}^{-2}\,\mathrm{s}^{-1}\,\mathrm{keV}^{-1}$, whilst mine lies at $\sim 6.4 \times 10^{-3}\,\mathrm{cm}^{-2}\,\mathrm{s}^{-1}\,\mathrm{keV}^{-1}$. This systematical difference of $\sim$ 5% might result from the different software used. Whilst I used the OSA software for my analysis, Jourdain and Roques (2020) used different software, e.g. XSPEC (Arnaud 1996) for the spectral fitting. Nevertheless, the relative values proceed in parallel, showing the compatibility of the result. Moreover, their results as well as mine lie within a 5% variability around the mean flux for the 24–50 keV and 50–150 keV energy bands, underlying the general stability of the Crab emission.
For the spectral analysis, Jourdain and Roques (2020) used 41 narrower energy bins

covering the 24–2200 keV energy domain and fitted the Band model (equation (23)) to their spectrum. As there is barely an overlap with the bins used by Jourdain and Roques (2020) and my HE energy range, I neglected the HE domain for the comparison. With this exclusion, I executed a new data analysis with the INTEGRAL OSA software for the exact same time frames used by Jourdain and Roques (2020): revolution 43-1196 and revolution 1214-2135. This was possible as a background model for the revolutions 2010 to 2135 is already available for the SE and PSD range, but not for the HE range. For the comparison of the two spectra for the respective time frames, I first gathered their data from Figure 4 (Jourdain and Roques 2020) and their best-fit parameters for the Band model from Table 2 (Jourdain and Roques 2020). Afterwards, I added my data to the plot. This is displayed in Figure 20a. One can see that my data, especially the SE spectrum, again is slightly higher than the spectrum of Jourdain and Roques (2020). Once more, this difference might result from the different software used for the data analysis. For the model fitting of the Band function, I was not able to replicate the plot of their band function with their best-fit parameters to their data as it clearly can be seen in Figure 20a. The Band model explicitly lies outside of the data points, especially when looking at the higher energy domain. The original figure of Jourdain and Roques (2020), to compare what the fit of the Band model is supposed to look, is shown in Figure 20b. The cause for this might be lying in the different software used for the spectral fitting (3ML vs. XSPEC used by Jourdain and Roques (2020)). Another potential reason for the difference is a problem with the normalization K (cf. equation (23)), because they do not report at which energy their given normalization is set.

This leads to the conclusion, that my results correspond with Jourdain and Roques (2020) for the biggest part of their paper. The same variation of the Crab emission as well as an overlap of the data points in the spectrum is visible with just the amplitude being off. However, the issue with the systematical offset of the flux values and the problem with the Band function fit has to be further investigated.

7. Conclusion

The goal of this thesis was to examine if the Crab can still be treated a standard candle in the X- and γ-ray energy domain. To answer this question, I constructed light curves and did a full spectral analysis of the Crab Nebula with the data provided by SPI since the beginning of the mission. In addition, I compared my results to the preceding work of Wilson-Hodge et al. (2011) and Jourdain and Roques (2009) and Jourdain and Roques (2020).

I have shown that the variability of the Crab emission is contained within 5% for the low energy bands from 24–150 keV (see Figure 10) for most of the data over the whole observation time of the Crab nebula (2003-2018). Furthermore, all light curves show a similar outcome, independent of the analytical methods (3ML, spimodfit, Bayesian Blocks) applied, supporting the robustness of my results. Moreover, my results also agree with Jourdain and Roques (2020), who also found a variability of 5% of the Crab emission from 2003 to 2019. The unchanged variability over the whole observation time, also demonstrates the nearly unchanged SPI germanium detector efficiency (within 5%) up to 400 keV, cf. Jourdain and Roques (2020). In addition, I could confirm both the decrease in the Crab flux from $\sim$ 2008 to 2010 discovered by Wilson-Hodge et al. (2011) and the decrease from $\sim$ 2015 to 2017, which is also visible in the light curves of Jourdain and Roques (2020). For the higher energy bands (400–8000 keV) no trends of the Crab emission temporal evolution could be identified.

Looking at the spectral shape of the Crab Nebula, I analyzed the mean spectrum of the Crab from revolution 43 to 2010 in the energy range 24–8000 keV (Figure 14) and compared three different fitting models (Figure 15). For this, I introduced a new model with a broken power-law with two break-energies (cf. equation 24) providing a better fit than a normal broken power-law with one break-energy (equation (22)) or the Band model (equation (23)). The break-energies at $x_{b1} \approx 100\,\text{keV}$ and $x_{b2} \approx 300\,\text{keV}$ suggest an additional structure superimposed to the power-law component, which has yet to be further investigated.

Additionally, I investigated the individual spectra per revolution fitted with a single broken power-law with a fixed break energy at $x_b = 100\,\text{keV}$ and looked at the evolution of the best-fit parameters (Figure 16), specifically the low- and high-energy slope α and β, respectively. The measured values are contained within 1σ of the weighted mean values $\alpha_{mean} = -2.08 \pm 0.03$ and $\beta_{mean} = -2.27 \pm 0.18$, indicating a stability of the Crab emission in shape. Furthermore, they are consistent with the resulting parameters of the mean spectrum and the best-fit parameters of the separate analysis with the Bayesian Blocks method. These values are within 2σ for α and 1σ for β compared to previous results by Jourdain and Roques (2009). Moreover, the variability of the Crab flux seen in the light curves and the evolution of the best-fit parameters in all energy bands seem to be barely correlated, because only a small direct correlation was observed.

To conclude, the Crab Nebula seems to be stable in X- and γ-ray emission, supporting it current status as the best standard candle in this energy region. However, the variations of the Crab flux intensity should be treated with caution and be further monitored, so that the Crab can safely be used as calibration source. As the reason for the variability of the Crab at all is still unknown, a perspective for a future work might be the search for any connections and maybe even a periodical behavior in the de- and increase of the Crab emission, when more long term data is available.

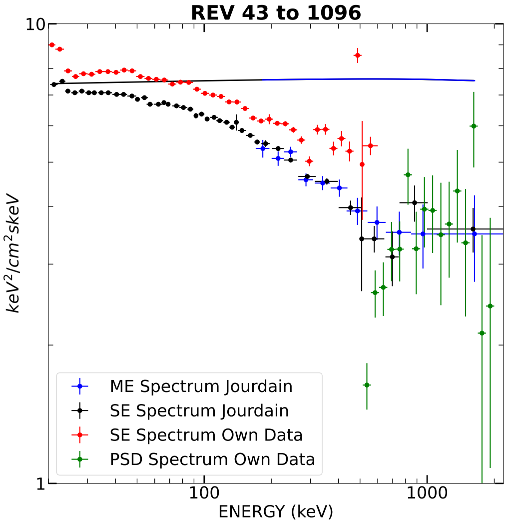

(a) Displayed in black and blue is the SE and ME spectrum of the Crab Nebula measured by Jourdain and Roques (2020). The black and blue lines are the Band model fit for the SE and ME spectrum, respectively, with the best-fit parameters of Jourdain and Roques (2020). For comparison, I also added my data for the same time intervals of the Crab emission, shown in red and blue for the SE and PSD spectrum.

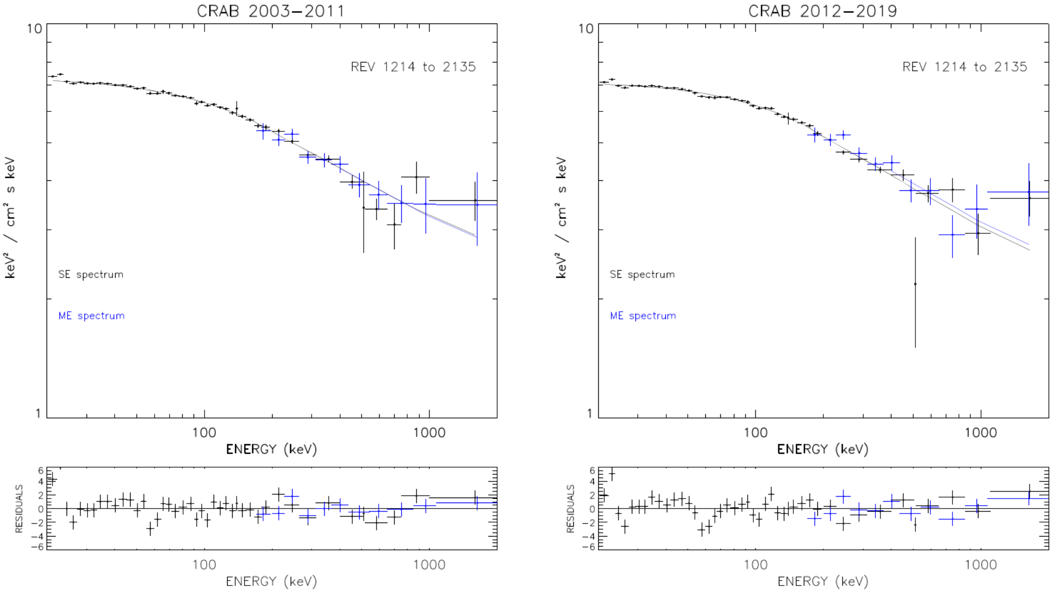

(b) Figure 4 of Jourdain and Roques (2020). The Crab spectra is separated in one-detector events (black points) and double-detector events (blue points). The black and blue lines represent the fitted Band model.

Figure 20: Comparison of the spectra received by Jourdain and Roques (2020, cf. Figure 4) with the spectra I received with the OSA software for the same time intervals. The spectrum is separated in two time frames, revolution 43-1096 (2003-2011) and revolution 1214-2135 (2012-2019).

A. Appendix

A.1. Further Lightcurves

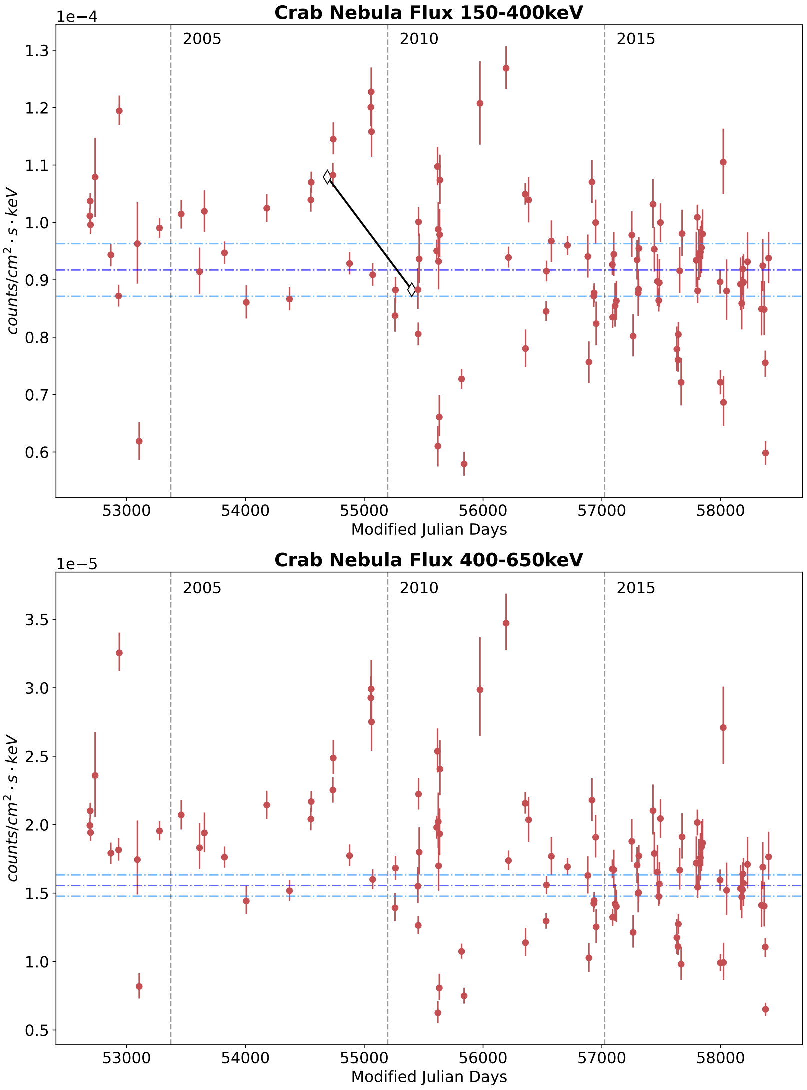

Figure 21: Similar to the description from Figure 10 with different energy bands. Top: Light curve in the 150–400 keV range. The black line pictures the source decline reported by Wilson-Hodge et al. (2011) from MJD 54690 to MJD $\sim$ 55400 with a total slope of $\sim$ 18%. Bottom: Light curve in the 400–650 keV range.

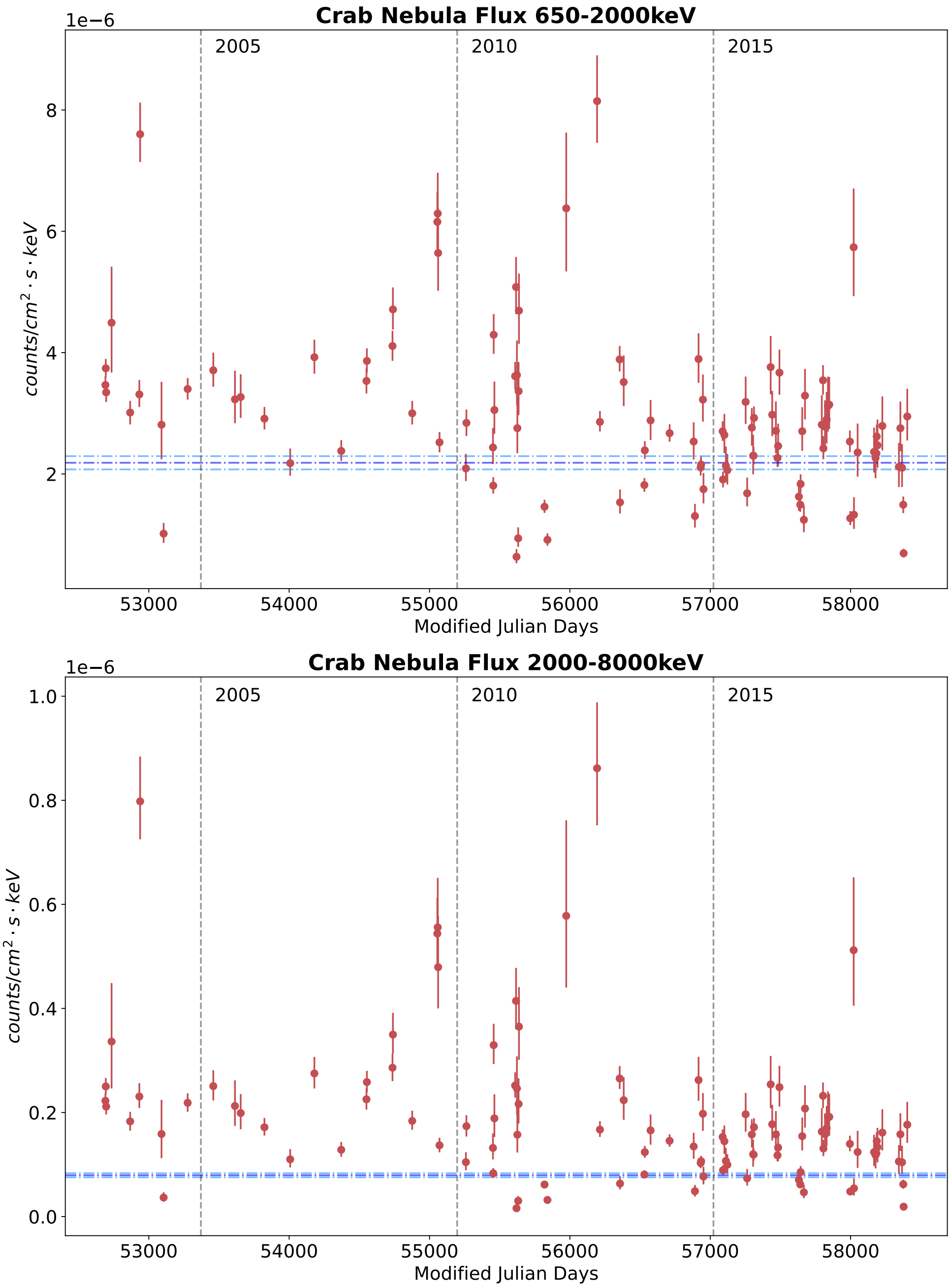

Figure 22: Similar to the description from Figure 10 with different energy bands. Top: Light curve in the 650–2000 keV range. Bottom: Light curve in the 2000–8000 keV range.

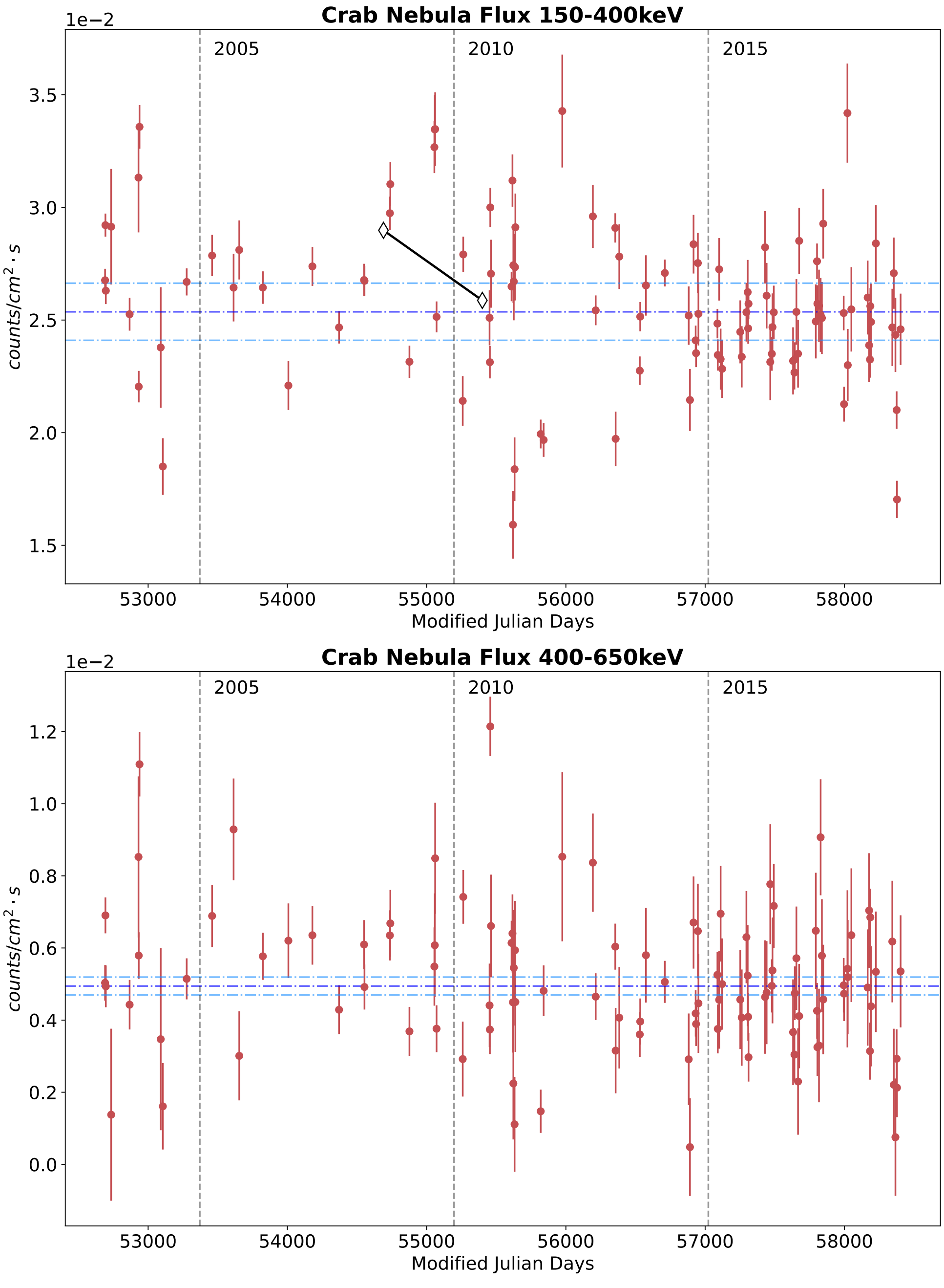

Figure 23: Similar to the description from Figure 21, but here the flux data per revolution has been retrieved directly from the spimodfit result instead of after the 3ML spectral fitting. Top: The black line pictures the source decline reported by Wilson-Hodge et al. (2011) from MJD 54690 to MJD $\sim$ 55400 with a total slope of $\sim$ 11%.

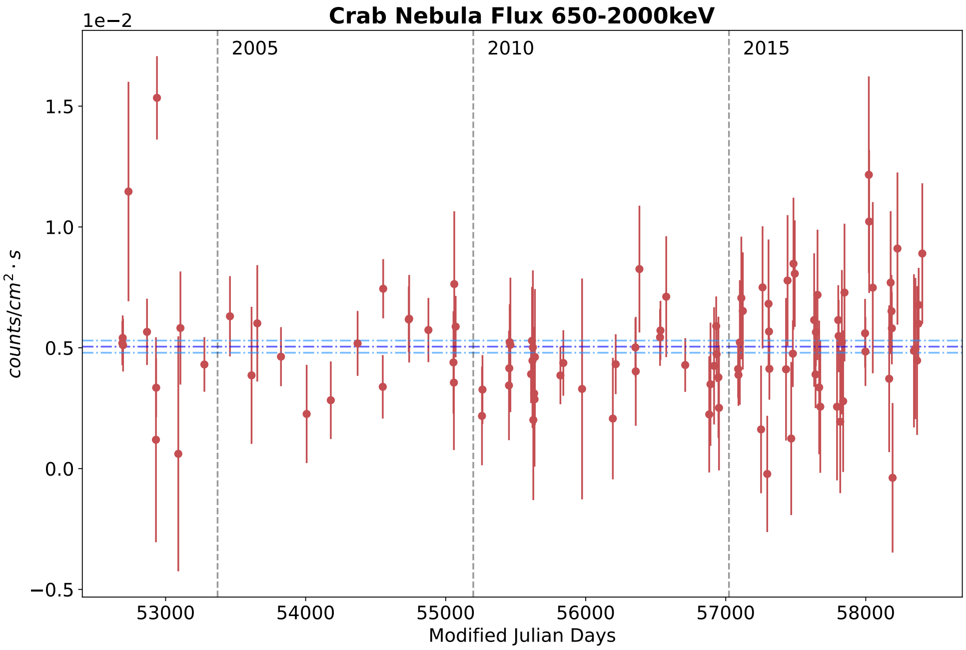

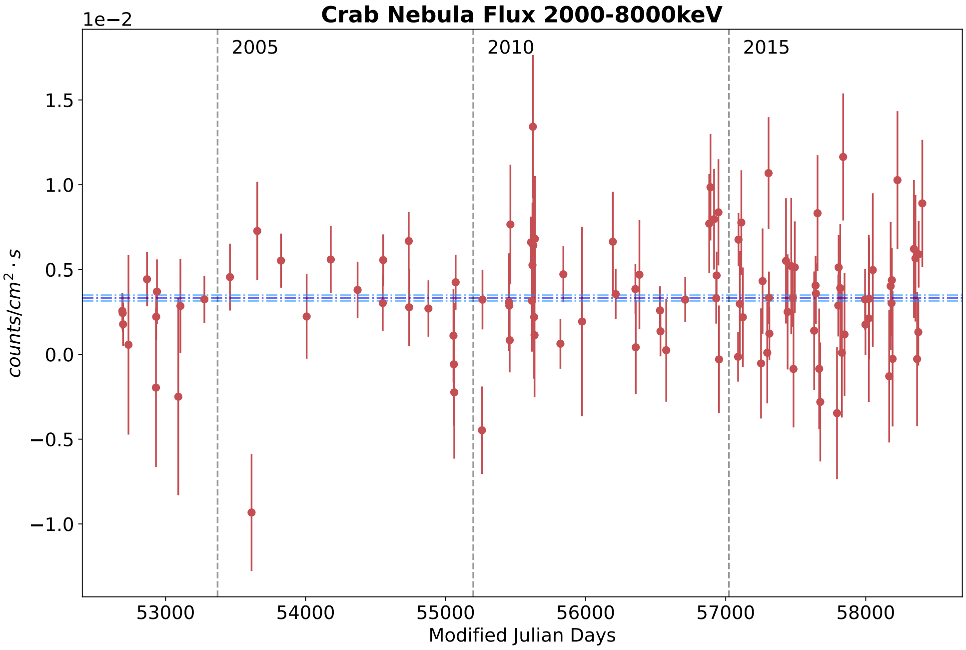

Figure 24: Similar to the description from Figure 22, but here the flux data per revolution has been retrieved directly from the spimodfit result instead of after the 3ML spectral fitting.

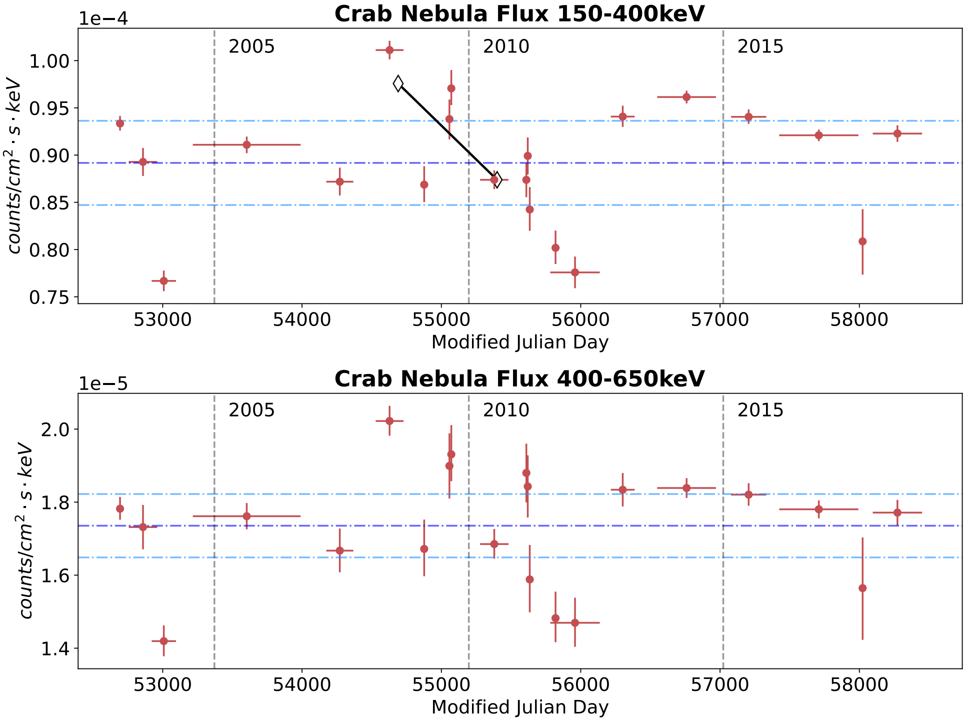

Figure 25: Similar to the description from Figure 21. Here data points with similar flux value have been merged together through the usage of the Bayesian blocks method and a separate data analysis with the INTEGRAL OSA software for the combined revolutions has been executed. Hence, a red data point represents the average flux value over the whole time frame of the x-error bar. Top: The black line pictures the source decline reported by Wilson-Hodge et al. (2011) from MJD 54690 to MJD $\sim$ 55400 with a total slope of $\sim$ 11%

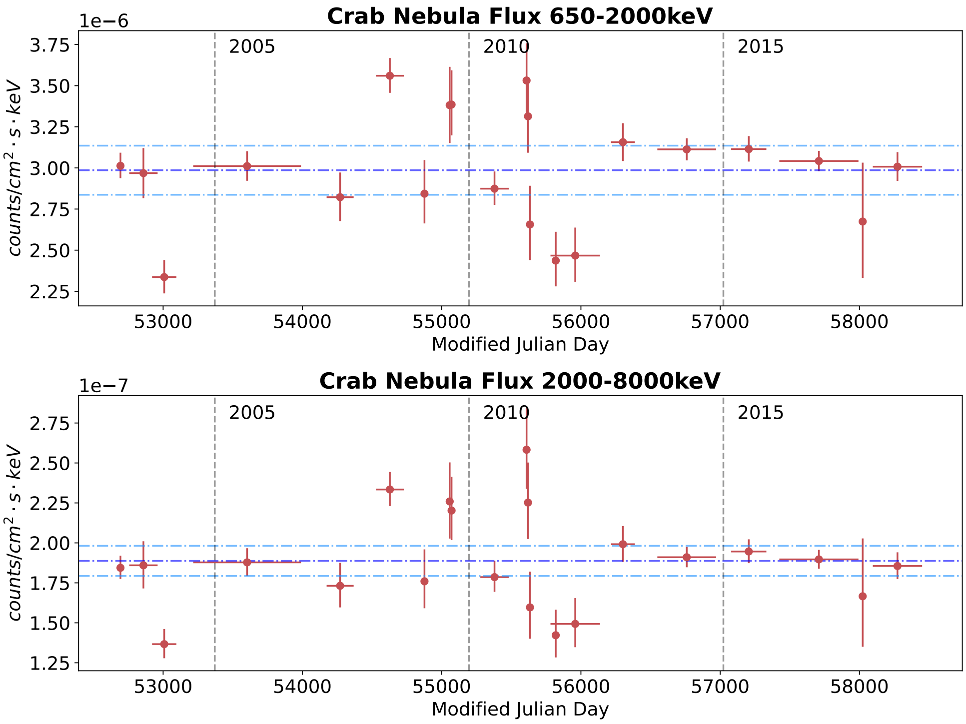

Figure 26: Similar to the description from Figure 22. Here data points with similar flux value have been merged together through the usage of the Bayesian blocks method and a separate data analysis with the INTEGRAL OSA software for the combined revolutions has been executed. Hence, a red data point represents the average flux value over the whole time frame of the x-error bar.

References

Akaike, H. (1974). “A new look at the statistical model identification”. In: *IEEE Transactions on Automatic Control* 19.6, pp. 716–723. DOI: `10.1109/TAC.1974.1100705`.

Al Dallal, S., W. J. Azzam, et al. (2021). “A Brief Review of Historical Supernovae”. In: *International Journal of Astronomy and Astrophysics* 11.01, p. 73. DOI: `10.4236/ijaa.2021.111005`.

Arnaud, K. (1996). “Astronomical data analysis software and systems V”. In: *ASP Conf.* Vol. 17. URL: `https://cir.nii.ac.jp/crid/1572543023972805376`.

Band, D. et al. (1993). “BATSE observations of gamma-ray burst spectra. I-Spectral diversity”. In: *The Astrophysical Journal* 413, pp. 281–292. DOI: `10.1086/172995`.

Biltzinger, B., J. Greiner, J. M. Burgess, and T. Siegert (2022). “Improving INTEGRAL/SPI data analysis of GRBs”. In: *arXiv preprint arXiv:2201.10310*. DOI: `10.48550/arXiv.2201.10310`.

Cavanaugh, J. E. (1997). “Unifying the derivations for the Akaike and corrected Akaike information criteria”. In: *Statistics & Probability Letters* 33.2, pp. 201–208. DOI: `10.1016/S0167-7152(96)00128-9`.

Courvoisier, T.-L. et al. (2003). “The INTEGRAL science data centre (ISDC)”. In: *arXiv preprint astro-ph/0308047*. DOI: `10.1051/0004-6361:20031172`.

Diehl, R. et al. (2018). “INTEGRAL/SPI γ-ray line spectroscopy-Response and background characteristics”. In: *Astronomy & Astrophysics* 611, A12. DOI: `10.1051/0004-6361/201731815`.

Duyvendak, J. (1942). “Further data bearing on the identification of the Crab Nebula with the supernova of 1054 AD Part I. The ancient oriental chronicles”. In: *Publications of the Astronomical Society of the Pacific* 54.318, pp. 91–94. DOI: `10.1086/125409`.

Gaensler, B. M. and P. O. Slane (2006). “The evolution and structure of pulsar wind nebulae”. In: *arXiv preprint astro-ph/0601081*. DOI: `10.1146/annurev.astro.44.051905.092528`.

Halloin, H. (2009). *spimodfit Explanatory Guide and Users Manual*. `https://www.isdc.unige.ch/integral/download/osa/doc/11.0/spimodfit_handbook.pdf`. Accessed: 2022-08-19.

Hanslmeier, A. (2014). *Einführung in Astronomie und Astrophysik*. Vol. 3. Springer. ISBN: 978-3-642-37700-6. DOI: `10.1007/978-3-642-37700-6`.

Hester, J. J. (2008). "The Crab Nebula: an astrophysical chimera". In: *Annu. Rev. Astron. Astrophys.* 46, pp. 127–155. DOI: `10.1146/annurev.astro.45.051806.110608`.

Hester, J. J., P. Scowen, and NASA (1996). *HUBBLE ASTRONOMERS UNVEIL "CRAB NEBULA – THE MOVIE"*. `https://hubblesite.org/contents/news-releases/1996/news-1996-22.html`. Accessed: 2022-08-31.

INTEGRAL Science Data Centre (2022). `https://www.isdc.unige.ch/integral/archive`. Accessed: 2022-08-20.

Jourdain, E. and J. P. Roques (2009). "The high-energy emission of the Crab Nebula from 20 keV TO 6 MeV with integral SPI". In: *The Astrophysical Journal* 704.1, p. 17. DOI: `10.1088/0004-637X/704/1/17`.

Jourdain, E. and J. P. Roques (2020). "2003–2019 Monitoring of the Crab Emission through INTEGRAL SPI, or Vice Versa". In: *The Astrophysical Journal* 899.2, p. 131. DOI: `10.3847/1538-4357/aba8a4`.

Knoll, G. F. (2011). *Radiation detection and measurement*. John Wiley & Sons, p. 864. ISBN: 978-0-470-13148-0.

Kretschmar, P. et al. (2005). "The INTEGRAL mission–an overview". In: *Proceedings of the International Astronomical Union* 1.S230, pp. 59–65. DOI: `10.1017/S1743921306007873`.

Mayall, N. U. (1939). "The Crab Nebula, a probable supernova". In: *Leaflet of the Astronomical Society of the Pacific* 3.

Mayall, N. and J. Oort (1942). "Further data bearing on the identification of the Crab Nebula with the supernova of 1054 AD Part II. The astronomical aspects". In: *Publications of the Astronomical Society of the Pacific* 54.318, pp. 95–104. DOI: `10.1086/125410`.

NASA, ESA, and Allison Loll/Jeff Hester (Arizona State University).Acknowledgement: Davide De Martin (ESA/Hubble) (2005). *Most detailed image of the Crab Nebula*. `https://esahubble.org/images/heic0515a/`. Accessed: 2022-08-31.

NASA and Night Sky Network (2009). *Life cycle of stars*. `https://nightsky.jpl.nasa.gov/download-view.cfm?Doc_ID=393`. Accessed: 2022-08-31.

Petry, D., V. Beckmann, H. Halloin, and A. Strong (2009). "Soft gamma-ray sources detected by INTEGRAL". In: *Astronomy & Astrophysics* 507.1, pp. 549–571. DOI: `10.1051/0004-6361/200912844`.

Press, W. H., S. A. Teukolsky, W. T. Vetterling, and B. P. Flannery (1992). *Numerical recipes in Fortran 77: The Art of Scientific Computing*. Cambridge University Press. ISBN: 0-521-43064 -X.

Roberts, N., D. Lorimer, M. Kramer, et al. (2005). *Handbook of pulsar astronomy*. Vol. 4. Cambridge University Press. ISBN: 9780521828239.

Rossi, B. (1969). *The Crab Nebula ancient history and recent discoveries*. Tech. rep.

Sarang (2016). *Proton-Proton branch 1 reaction*. `https://commons.wikimedia.org/wiki/File:Fusion_in_the_Sun.svg`. Accessed: 2022-08-31.

Scargle, J. D. (1998). "Studies in astronomical time series analysis. V. Bayesian blocks, a new method to analyze structure in photon counting data". In: *The Astrophysical Journal* 504.1, p. 405. DOI: `10.1086/306064`.

Siegert, T. et al. (2019). "Background modelling for γ-ray spectroscopy with INTEGRAL/SPI". In: *Astronomy & Astrophysics* 626, A73. DOI: `10.1051/0004-6361/201834920`.

Vedrenne, G. et al. (2003). "SPI: The spectrometer aboard INTEGRAL". In: *Astronomy & Astrophysics* 411.1, pp. L63–L70. DOI: `10.1051/0004-6361:20031482`.

Vianello, G., J. M. Burgess, N. D. Lalla, N. Omodei, and H. Fleischhack (2021). *3ML*. `https://threeml.readthedocs.io/en/stable/`. Accessed: 2022-08-22.

Wilson-Hodge, C. A. et al. (2011). "When a standard candle flickers". In: *The Astrophysical Journal Letters* 727.2, p. L40. DOI: `10.1088/2041-8205/727/2/L40`.

Winkler, C. et al. (2003). "The INTEGRAL mission". In: *Astronomy & Astrophysics* 411.1, pp. L1–L6. DOI: `10.1051/0004-6361:20031288`.

List of Figures

List of Tables